Large influence of vacancies on the elastic constants of cubic epitaxial tantalum nitride layers grown by reactive magnetron sputtering

Grégory Abadias, Chen-Hui Li, Laurent Belliard, Qing Miao Hu, Nicolas Grenèche, Philippe Djemia

Version of Record: https://www.sciencedirect.com/science/article/pii/S1359645419307803
Manuscript_d4eb37a72eafab438db66287b2ef62ae

Large influence of vacancies on the elastic constants of cubic epitaxial tantalum nitride layers grown by reactive magnetron sputtering

Grégory Abadias[a]*, Chen-Hui Li[b]*, Laurent Belliard[c], Qing Miao Hu[d], Nicolas Greneche[b], Philippe Djemia[b]

[a]*Institut Pprime, UPR 3346, CNRS-Université de Poitiers-ENSMA, SP2MI, TSA 41123, F86962 Futuroscope-Chasseneuil, France*

[b]*Laboratoire des Sciences des Procédés et des Matériaux, UPR 3407 CNRS, Université Paris 13, Sorbonne Paris Cite, 99 Avenue J.B. Clément 93430 Villetaneuse, France*

[c]*Sorbonne Université, CNRS, UMR 7588, Institut des NanoSciences de Paris, 4 Place Jussieu, 75252 Paris Cedex 05, France*

[d]*Institute of Metal Research, Chinese Academy of Sciences, Wenhua Road 72, Shenyang 110016, P. R. China*

Abstract: We report a comprehensive study on the structure and elastic constants of epitaxial cubic δ-Ta_xN (x≈1) layers deposited by reactive magnetron sputtering at 570°C on MgO(001), MgO(110) and MgO(111) substrates. X-ray diffraction shows that all layers are single-phase and have a single-crystal rocksalt-structure, growing with an epitaxial cube-on-cube relationship with respect to their MgO substrates. For (001)-orientation, Brillouin light scattering provides the measurement of c_{44} (137 ± 3 GPa) and c_{12} (130 ± 5 GPa) single-crystal elastic constants, while picosecond laser ultrasonics (PLU) provides the third independent one, c_{11} (530 ± 10 GPa). For (110)- and (111)-orientations, PLU provides selectively the following combinations, $(c_{11}+c_{12}+2c_{44})/2$ and $(c_{11}+2c_{12}+4c_{44})/3$, respectively. Electrical resistivity measurements show evidence of point defects in the films despite a composition close to 1:1 stoichiometry. Point defects (metal and nitrogen vacancies) are considered in our first-principles calculations to find closer agreement between experimental and theoretical lattice parameter, mass density, sound velocities and elastic constants. Sound velocities and elastic constants are found to be particularly sensitive to the presence of vacancies, resulting into a more compliant and less anisotropic material. While only ~ – 1 % mismatch is found between predicted defect-free and experimental lattice parameters, huge differences of –27 % and +180 % are observed for c_{11} and c_{44},

respectively. These discrepancies can be rationalized by considering the presence of point defects (metal vacancy and/or Schottky defect) in concentration ~11% in the as-deposited TaN films, a compositional value that corresponds to the lowest formation energy of δ-TaN_x structure.

Keywords: Nitrides, Thin Films, Elastic constants, point defects, ab initio calculations

* corresponding authors: Gregory Abadias, gregory.abadias@univ-poitiers.fr; Chen-Hui Li, lichcn1@gmail.com

1. Introduction

Due to their unique electronic band structure and refractory character, transition metal nitrides (TMNs) are a fascinating class of materials which combine high strength (bulk modulus *B* and hardness *H*), chemical and thermal stability, and exhibit a wide range of electronic and optical properties [1,2]. Many MeN_x thin films, where Me is an early transition metal belonging to group 4 to group 6, crystallize in their cubic, rocksalt structure (space group of $Fm\bar{3}m$ symmetry) and exist in a large compositional field, covering both under- and over-stoichiometric compositions. Long known and amply used as protective and hard coatings in the cutting tools industry [3,4], TMN layers are also integrated in microelectronic and optoelectronic devices [5]. Besides, they are currently generating further interest as perspective materials for plasmonics [1,6–8], thermoelectrics [9–11] and energy storage and conversion [12,13].

As far as the mechanical properties are concerned, MeN_x thin films of group 5 (VN, NbN, TaN) and group 6 (CrN, MoN and WN) have recently been the subject of active investigations because they offer improved ductility compared to inherently brittle TiN or ZrN coatings, while retaining a high hardness [14–20]. Thus, alloy design strategies based on the formation of metastable, cubic multicomponent TMN solid solutions by incorporation of

group-5 or group-6 metals, or tailoring of interfaces in superlattices, have been proposed for toughness enhancement [21–30]. Such toughening has been predicted to be originating from an increase in valence electron concentration [15,31], and was confirmed experimentally in a few systems either from a direct observation of nanoindentation imprints [17,32], improvement in the hardness over Young's modulus (H/E) ratio [16,27,29] or assessment of their elastic constants [24,25].

Of particular interest is the cubic δ-TaN compound, which exhibits the highest hardness (30-33 GPa) among TMN binaries [33,34]. However, there exists a large discrepancy in the literature regarding phase stability, lattice parameters and mechanical properties of polycrystalline TaN_x thin films. For instance, published values of the lattice parameter range from 4.33 to 4.42 Å. Djemia *et al*. reported [35] shear modulus values ranging from 95 to 257 GPa for sputter-deposited TaN films depending on the Ar working pressure. A large spread in hardness values, from 25 to 42 GPa, is also noticed for polycrystalline TaN_x layers [33]. This is likely related to the fact that the Ta-N system is inherently complex, comprising a large variety of stable and metastable phases [36,37]. Therefore, the mechanical behavior of polycrystalline TaN_x films is anticipated to be extremely sensitive to the growth conditions which affect chemical and phase compositions, as well as microstructures. Besides, the elastic properties are expected to be crystal-orientation dependent, based on *ab initio* calculations of single-crystal elastic constants of δ–TaN compound [14,24,31,35]. This motivates the need for further investigations of the structure and elastic properties of well-characterized single-phase TaN layers.

The TaN compound (1:1 stoichiometry) exists in three stable forms, depending on temperature and pressure conditions [36,38]. The hexagonal ε-phase (space group of $P\bar{6}2m$) is found to be most stable at room temperature [39], closely followed by the θ-phase (space group of $P\bar{6}m2$, WC-type) observed at high pressure [40]. The δ-TaN compound with cubic

symmetry (space group of $Fm\bar{3}m$, NaCl-type) is typically stabilized at high temperatures. This cubic phase is highly anisotropic (Zener'anisotropy ratio ~0.20 [14,35]) and would support theoretically a large density of vacancies up to 20% [41]. Using density functional theory (DFT) Kim *et al*. [38] calculated the electronic and structural properties of these three stoichiometric tantalum mononitride phases. Interestingly, they first reported that the cubic δ-TaN phase undergoes a spontaneous distortion into a tetragonal structure (δ'-TaN, space group of P4/nmm), with a reduced metal interatomic distance, $d_{Ta–Ta}$, by as much as 0.155 Å in the plane normal to the c-axis (ab-plane). This geometric distortion alters the degeneracy of Ta-*d* orbitals at the Fermi level, lowering the overall energy of the system. However, the metallic bonding character is the highest for δ-TaN phase.

Balasubramanian *et al*. [42] demonstrated that both under-stoichiometric ($x < 1$) and over-stoichiometric ($x > 1$) TaN_x compositions are due to relatively low vacancy formation energies of ~0 and −3.4 eV/defect for N and Ta, respectively, indicating that both vacancies are thermodynamically stable at 0 K. On the other hand, point defects of interstitial or antisite types are unstable in TaN, especially for Ta interstitials or Ta atoms at substitutional sites, corresponding to high formation energies (> 6.0 eV). Koutná *et al*. [41,43] also predicted that sub-stoichiometric δ-TaN_x structures are more stable, with $Ta_{0.78}N$ (~11% Ta vacancies) having the lowest formation energy of −2.1 eV/(f.u.). They also reported that the introduction of Schottky defects (consisting of cation + anion vacancy pair) significantly lowers the formation energy of δ-TaN, without altering the stoichiometry. Structures containing Schottky defects yield smaller lattice constants [41] and hence may contribute to explain the relatively large scatter of experimental data. Additionally, the stability of each defect type in MeN_x compounds is predicted to depend on the thermodynamic conditions (N_2 partial pressure and deposition temperature) [42].

From the literature survey outlined above, it is clear that point defects decisively affect the compositional variations and structural parameters in many rocksalt structure MeN_x compounds, especially for group 4-6 nitrides. However, their impact on the elastic properties remains to date unexplored. In the present work, we contribute to address this issue by combining experimental assessment and DFT-based calculations of the elastic constants of epitaxial δ-TaN_x layers with different crystallographic orientations. We systematically study the influence of vacancies on the phase stability, structure, sound velocities and elastic properties of various Ta_yN_x compounds over a wide range of defect concentration (up to x,y=0.6). We specifically discuss the case of Schottky pair as a defect structure consisting of an anion and a cation vacancy. Its formation or annihilation does not affect the overall composition and should be considered because our produced films were found to be nearly stoichiometric.

2. Experimental procedure and computational modelling

2.1. Thin film deposition

TaN films (~150 nm thick) were grown by direct current (DC) reactive unbalanced planar magnetron sputtering in a load-locked high-vacuum (base pressure < 8×10^{-6} Pa) chamber with a target-to-substrate separation of 18 cm. Films were deposited in the same batch on single-crystal MgO(001), MgO(110) and MgO(111) substrates (1×1 cm^2) at a growth temperature T_s=570°C and using a constant substrate bias voltage of –60 V. A 3-inch Ta (99.998 % purity) target was sputtered at constant DC power (200 W) in an Ar (35 sccm)-N_2 (4 sccm) plasma discharge at a total pressure of 0.65 Pa, the N_2 gas being injected in the close vicinity of the substrate via a circular ring. The N_2 flow rate (corresponding to a N_2 partial pressure of 0.05 Pa, as measured using a MKS Microvision mass spectrometer) was adjusted so as to obtain stoichiometric TaN films, based on our earlier studies on the growth of polycrystalline TaN

films on Si [35,44]. Prior to deposition, the MgO substrates were heated to 800°C during 1 h and then exposed to plasma etching with 60 eV Ar ions during 2 min to remove surface contamination. Deposition time of TaN films was 25 min, with the substrate holder being rotated at 10 rpm to ensure a uniform deposition rate.

2.2 Composition, structure and electrical conductivity

Elemental composition was investigated by wavelength-dispersive X-ray spectroscopy (WDS) microanalysis unit from Oxford Instruments attached to a JEOL-7001F-TTLS scanning electron microscopy operated at 10 kV. The Ta M_α line was used for the intensity measurement of tantalum, while for nitrogen, a reference AlN standard was used for calibration of the N K_α line.

The crystal structure and crystal orientation were characterized by X-ray diffraction (XRD) using a four-circle Seifert XRD 3000 diffractometer equipped with Cu tube, operated under different configurations. θ–2θ scans were recorded in line focus mode using a monochromatic beam (Cu $K\alpha_1$ radiation of wavelength λ= 0.15406 nm obtained from a two-crystal Ge(220) monochromator) and a scintillation detector defined by an opening angle of 0.018° as secondary optics. The same parallel beam configuration was also used to collect reciprocal space map (RSM) around asymmetric 113 reflection of the TaN/Mg(001) film, using a 0.05°divergence detector slit. Pole figures, off-axis φ-scans and ω-rocking curves were acquired using the Seifert XRD 3000 diffractometer operating in point focus mode with Cu K_α radiation (wavelength λ= 0.15418 nm), a Ni filter to remove Cu K_β reflections, and a scintillation detector defined with an acceptance angle of 0.21°.

X-ray reflectometry (XRR) was employed to determine the thickness *t*, mass density ρ and surface roughness η of the TaN films. Scans were recorded using the Seiffert XRD 3000 diffractometer in line focus mode using the same primary and secondary optics as θ–2θ scans described above. XRR scans were fitted to theoretical curves calculated from the optical

formalism of Parratt [45] using Analyze proprietary software and assuming a three layer model (surface layer/TaN film/ MgO substrate).

The room temperature (RT) electrical resistivity ρ_{el} was measured using a standard four-point probe set-up, with Van der Pauw configuration. Measurements were made through spring-loaded contact tips, using 1 mA current.

2.3. DFT calculations

The Vienna Ab-initio Simulation Package (VASP) [46,47] was used to perform the DFT calculations, employing the projector augmented plane wave pseudopotentials under the generalized gradient approximation (GGA) [48] with a Perdew-Burke-Ernzerhof exchange and correlation functional [49]. The valence electron configuration is $5p^6\ 5d^3\ 6s^2$ for Ta and $2s^2\ 2p^3$ for N. A 2×2×2 cubic supercell consisting of 64 lattice sites is chosen to model the defected Ta_xN and TaN_x compounds ($x \leq 1$). The plane-wave cutoff energy was always set to 800 eV and the 8×8×8 Monkhost-Pack *k*-vector sampling of the Brillouin zone was checked to provide a total energy accuracy of about 1 meV/at, elastic stress tensor convergence within 2 kbar and the elastic constants convergence within 10 GPa, for tested configurations. Atomic positions as well as shape and volume of the unit cell were allowed to relax.

To compare various systems in terms of their thermodynamic stability, the formation energy, E_f, was calculated as

$$E_f = \frac{1}{\sum_s n_s}(E_{tot} - \sum_s n_s \mu_s) \quad (1)$$

where E_{tot} is the total energy of the supercell, n_s and μ_s are the number of atoms and the chemical potential, respectively, of bulk reference species s = Ta or N. The reference chemical potentials for Ta and N are conventionally set to the total energy per atom of bcc-Ta, μ_{Ta} (−11.804 eV/at.), and N_2 molecule, μ_N (−8.322 eV/at.), respectively. The TaN defect-free structure was proposed by Balasubramanian *et al*. [42] as another reference choice

considering it is more relevant in the case of thin film growth. In this case, the formation energy is lowered by the tantalum chemical potential difference, $\Delta\mu_{MS} = \mu_{Ta} - \mu_{TaN} = 1.768$ eV/at., between bcc-Ta and TaN reference states ($\mu_{TaN} = -13.572$ eV/at).

Moreover, several defected or non-stochiometric structures were investigated with different degree of ordering/clustering of the metal cation or nitrogen anion vacancy. Metal vacancies, nitrogen vacancies and Schottky defects (containing equivalent number of metal and nitrogen vacancies) were considered as possible defects. DFT calculations have been carried out for a defect concentration up to 20%, the defect concentration being evaluated with respect to the total (metal + nitrogen) lattice sites. With this definition, one has to bear in mind that the number of Schottky defects is actually twice as for Ta or N vacancies, for a given defect concentration in supercell. The Alloy Theoretic Automated Toolkit (ATAT) was employed to generate the special quasi-random structures (SQS) [50], representing random distribution of vacancies (denoted as "random" configuration). The short-range order parameters were optimized for pairs up to seventh order and to fifth order for triplets. Besides, we considered ordered distribution of vacancies (denoted as "symmetric" configuration) by removing atoms with certain site symmetries from the 2×2×2 supercell. Hence, in the symmetric configurations, all the defected structures remain cubic. Finally, to evaluate the vacancy clustering effect, we simulated certain cluster configurations, by removing the neighboring cations or anions in the supercell. In the case of Schottky-type defects, SQS were again adopted to remove randomly identical number of metal and nitrogen atoms.

We searched for additional stable structures offering ordered Ta and N vacancies with different concentrations by employing the UNiversal CLuster Expansion (UNCLE) code [51]. The identified structures and their properties are described in the Supplementary Material (see **Fig. S3** and **Table S4**) [52]. This complementary approach based on cluster expansion (CE) calculations enabled us to scrutinize the 0-25% ordered-vacancy concentration interval.

The lattice constant a of defected δ-TaN structures was calculated from $a = (V_0)^{1/3}$, where V_0 is the equilibrium volume corresponding to the conventional cubic cell. Our structural models are based on 2×2×2 supercells constructed from the conventional cubic cells, therefore we took $V_0 = V/8$ where V is volume of the fully relaxed supercell with or without defect(s). Due to supercell finite size effect, the relaxed defected supercells do not have, in general, cubic shape anymore. However, the defected materials will macroscopically possess the cubic symmetry, so that evaluating a from the supercell volume will effectively average the local atomic distortions and provide the correct estimation of the lattice constant for the macroscopically cubic material.

We investigated elasticity of selected TaN_x structures by employing the stress-strain method [53,54]. Fourth-order elasticity tensor c relates the stress, σ, linearly to the strain, ε, according to the Hooke's law

$$\sigma = c\varepsilon \tag{2}$$

By convenience, instead of using the fourth-order tensor c in a three-dimensional space, it is often replaced by a 6×6 matrix. In the following, c will represent this matrix of elastic constants in the so-called Voigt's notation. To evaluate elastic constants corresponding to structures with arbitrary symmetry, we adopt the methodology proposed by Moakher and Norris [55]. First, the squared norm of the elasticity matrix c is defined as

$$\|c\|^2 = (c, c) \tag{3}$$

The scalar product (c, c) can be calculated in various ways depending on how c is represented. Assuming the Euclidean metrics and the case of 2D representation, Eq. (3) takes the form

$$\|c\|^2 = \sum_{i,j}^{6} c_{ij}^2 \tag{4}$$

Simplifying the general 6×6 matrix $c = (c_{ij})$ with 21 independent constants, we must project it onto a convenient symmetry class and hence, decrease the number of independent

elastic constants. Thus, we search for a matrix c_{sym} of a specific symmetry class such that the norm $\|c - c_{sym}\|$ is minimal. Rigorous derivation of the projectors for all crystal symmetry classes can be found in Refs. [55,56]. In this work, we restricted the search to a cubic or a tetragonal symmetry when we used the SQS method.

$$\begin{pmatrix} \varepsilon & 0 & 0 \\ 0 & 0 & \frac{1}{2}\varepsilon \\ 0 & \frac{1}{2}\varepsilon & 0 \end{pmatrix} \& \begin{pmatrix} 0 & 0 & \frac{1}{2}\varepsilon \\ 0 & \varepsilon & 0 \\ \frac{1}{2}\varepsilon & 0 & 0 \end{pmatrix} \& \begin{pmatrix} 0 & \frac{1}{2}\varepsilon & 0 \\ \frac{1}{2}\varepsilon & 0 & 0 \\ 0 & 0 & \varepsilon \end{pmatrix} \tag{5}$$

To calculate the elastic constants, we employed the above deformation matrices with ε equals to ± 0.004, as in the stress-strain method. They are equivalent for materials of cubic symmetry. However, for the SQS structures we used, elastic tensor can barely maintain cubic symmetry due to randomly distributed vacancies. One usually gets elastic constants by averaging relevant elastic constants. For a cubic system with 3 independent elastic constants, we have the following averaging relations:

$$\bar{c}_{11} = \frac{1}{3}(c_{11} + c_{22} + c_{33}) \tag{6}$$

$$\bar{c}_{12} = \frac{1}{3}(c_{12} + c_{23} + c_{13}) \tag{7}$$

$$\bar{c}_{44} = \frac{1}{3}(c_{44} + c_{55} + c_{66}) \tag{8}$$

2.4. Measurement of elastic constants

Brillouin light scattering (BLS) was analyzed by means of a Sandercock-type 3 + 3 pass tandem Fabry-Perot interferometer, in the back-scattering geometry, considering the coupling of the incoming light (wave vector $\boldsymbol{k}_{\mathrm{I}}$ and frequency f_{I}) with the surface acoustic waves (wave vector $\boldsymbol{Q}_2$ and frequency f), see **Fig. 1**. The inelastic scattered light (wave vector $\boldsymbol{k}_{\mathrm{S}}$ and

frequency f_S) satisfies the conditions $\boldsymbol{k}_S = -\boldsymbol{k}_I$, $(\boldsymbol{k}_S - \boldsymbol{k}_I)_{\parallel} = \pm \boldsymbol{Q_2}$ and $f_S - f_I = f$. The surface acoustic waves (SAW) are propagating along one in-plane direction with a wave vector direction ($\boldsymbol{Q}_2$) and with a wave vector modulus $Q_2 = 4\pi\sin(\theta)/\lambda_L$, λ_L is the wavelength of the incident laser beam (532 nm) and θ the angle of incidence of the light with respect to the perpendicular z-axis. In our case of a non-transparent film, the bulk acoustic wave (wave vector $\boldsymbol{Q_1}$, see **Fig. 1**) cannot be observed [57].

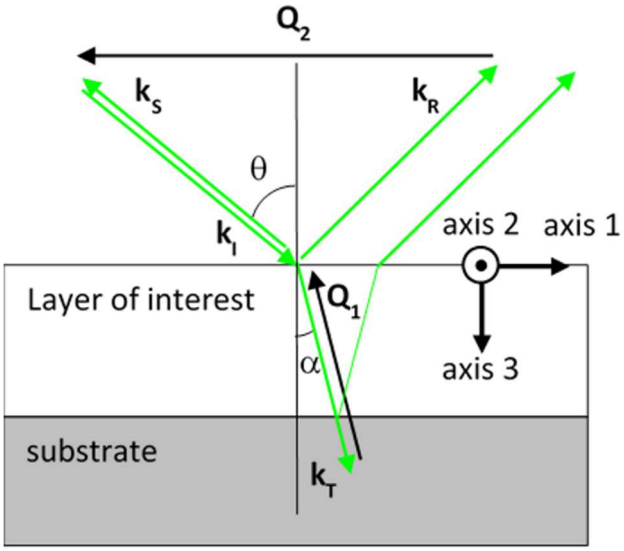

Figure 1 : Schematics of the Brillouin light scattering principle.

In the case of a "slow" film on a "fast" substrate ($V_T^{film} < V_T^{substrate}$), where V_T denotes the transverse sound velocity, both the Rayleigh surface wave (R) and the Sezawa standing waves (S_i) can be observed [25,58,59]. Frequencies (f) and sound wave velocities (V_{SAW}) are related by $V_{SAW} = 2\pi f/Q_2$. For thin films (thickness $t < 2\pi/Q_2$), V_{SAW} are dispersive as a function of $Q_2 \times t$. The BLS spectra were obtained at RT with a typical counting time of several hours. All spectra obtained for different θ in the 25°-80° range were fitted by considering the dynamical corrugation ($u_z(\omega = 2\pi f, z = 0)$) induced by the vertical atomic displacement u_z at the free surface, as being the active ripple mechanism responsible of the inelastic light scattering [25,60]. Cubic elastic properties of the epitaxial TaN films are

assumed, with three independent elastic constants c_{11}, c_{12} and c_{44} in the Voigt notation, and surface wave propagation along the [100] crystallographic direction for the TaN/MgO(001) film. The fitting of the Rayleigh surface wave line enables the precise determination of the shear elastic constant c_{44} and of V_T, through the relation $c_{44} = \rho(V_T)^2$, while fitting Sezawa waves provides c_{12} elastic constant if we consider c_{11} being fixed to the value determined by the picosecond laser ultrasonic (PLU) technique described hereafter.

Time-resolved measurements of longitudinal sound velocity V_L were performed using a standard PLU setup [61–63]. The pump and probe beams, emitted simultaneously by a mode-locked Ti:Sapphire Tsunami Spectra-Physics laser source operating at 800 nm with a repetition rate around 79.3 MHz, are focused by means of a long working distance lens on a 20 nm titanium thin film transducer. Following the modulated pump absorption, an ultrafast lattice deformation is induced, creating a coherent acoustic pulse at the free surface. This longitudinal acoustic wave propagating in the system along the z axis is partly transmitted and reflected back at the film/substrate interface and finally detected through the transient sample reflectivity change at the free surface using the time delayed probe beam. Knowing the sample thickness (t) and measuring the time of flight (TOF) in the film, the longitudinal sound velocity $V_L = 2t/\text{TOF}$ of the film could be obtained, and the longitudinal elastic constant along the growth axis $c_L = \rho(V_L)^2$ calculated. In case of the (001)-, (110)- and (111)-orientations, c_L is equal to c_{11}, $(c_{11}+c_{12}+2c_{44})/2$ and $(c_{11}+2c_{12}+4c_{44})/3$, respectively.

3. Results and discussion

3.1. Structural and physical properties: experiments

Elemental analysis by WDS shows that TaN layers have a Ta/N ratio close to 1, i.e., can be considered as stoichiometric. However, slight variations (±2 at.%) are measured depending on crystal orientation (see Table 1) and could reflect different defect concentrations in the

films. The RT electrical resistivity is found to be 252 ± 5 and 210 ± 5 μΩ.cm for the TaN/MgO(111) and $Ta_{0.93}N$/MgO(001) films, respectively. These values are consistent with reported values of 185 ± 15 [33], 225 ± 5 [64] and ~220 μΩ.cm [65] for epitaxial TaN_x layers with x~1.0. Over-stochiometric TaN_x epitaxial films with x>1.2 were found to be more resistive, reaching ρ_{el} = 310 μΩ.cm for x = 1.37 [66].

Sample	Film thickness *t* (nm)	Mass density ρ ($g.cm^{-3}$)	Surface roughness η (nm)	Ta/N	ρ_{el} (μΩ.cm)
$Ta_{0.93}N$/MgO(001)	154	15.6	0.7	0.93	210
$TaN_{0.99}$/MgO(110)	148	15.7	0.6	1.01	/
TaN/MgO(111)	/	/	> 2.5	/	252

Table 1: Physical properties of epitaxial TaN_x layers deposited on MgO substrates with different crystal orientations.

Figure 2 shows the XRR scans acquired on the different TaN/MgO samples. Despite that these films were deposited in the same run, differences in terms of mass density, film thickness and surface roughness were found depending on substrate orientation. One striking difference is the absence of Kiessig's fringes in the specular reflected beam from the film deposited on the MgO (111) substrate, together with stronger intensity decay. This is related to the poor surface finish quality of MgO(111) substrates [67–69], which exhibit rough triangular facets with exposed vicinal planes and suppress the constructive interferences between the reflected beams at the air/TaN layer and TaN layer/substrate interfaces. Therefore, it was not possible to extract information on the deposited thickness for this film. One can also notice for this sample a different shape of the reflected intensity near the critical angle $2\theta_c$, again related with the development of a rough TaN morphology and smeared-out density profile. In contrast, the $Ta_{0.93}N$/MgO(001) and $TaN_{0.99}$/MgO(110) films appear fully dense, as their critical angles were found to be very close to the value for bulk δ-TaN, $2\theta_c$ =

1° (with $\theta_c \propto \sqrt{\rho}$, and $\rho_{\delta-TaN}$ = 15.8 g.cm^{-3}). This is confirmed from the ρ values of 15.6 ± 0.2 and 15.7 ± 0.2 g.cm^{-3}, respectively, extracted from the best-fit simulations for these two samples (see **Fig. 2** and **Table 1**). The film thickness and surface roughness were *t*=154 nm and η=0.7 nm, and *t*= 148 nm and η=0.6 nm, for the TaN films deposited on MgO(001) and MgO(110), respectively. For the TaN/MgO(111) film, the surface roughness was significantly higher, > 2 nm (note that an accurate fit of the XRR curve could not be obtained for this sample).

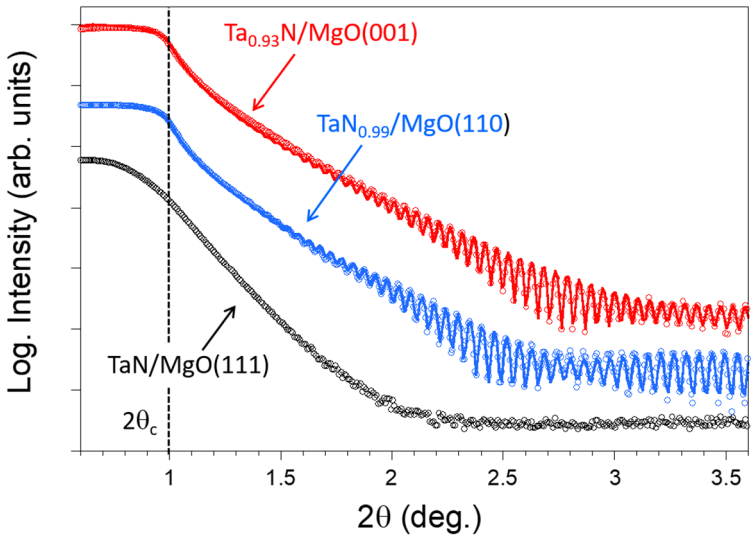

Figure 2: XRR scans from TaN/MgO(111), $Ta_{0.93}N$/MgO(001) and $TaN_{0.99}$/MgO(110) sputter-deposited films. The solid lines correspond to best-fit simulations to experimental data (open circles) using optical model of Parratt [45]. The vertical dashed line indicates the critical angle ($2\theta_c$) for bulk stoichiometric δ-TaN ($\rho_{\delta-TaN}$ = 15.8 g.cm^{-3})

The XRD patterns of the TaN/MgO(111), $Ta_{0.93}N$/MgO(001) and $TaN_{0.99}$/MgO(110) films are displayed in **Figure 3a**. For each film, only a single reflection is detected over the 2θ range between 30 and 65°, in addition to the XRD line from the single-crystal MgO substrate. The peaks, centered at 2θ = 35.22°, 40.85° and 59.41°, were indexed as B1 rocksalt

structure TaN 111, 002 and 220 reflections, respectively. This shows that single-phase cubic δ-TaN films were stabilized under the present deposition conditions.

Corresponding XRD {111} pole figures from TaN_x films grown on MgO(111), MgO(001) and MgO(110) are shown in **Fig. 3b** as stereographic projections across zenithal (ψ = 0–86°) and azimuthal (ϕ = 0–360°) angles, with diffracted intensity represented by isointensity contours. The pole figures of $Ta_{0.93}N$/MgO(001) and $TaN_{0.99}$/MgO(110) films exhibit the characteristic patterns of single-crystal materials with cubic structure: on MgO(001), four {111} peaks are observed, separated by 90° in ϕ and tilted at ψ~55.0° from the surface normal, corresponding to the 111, $\bar{1}11$, $1\bar{1}1$ and $\bar{1}\bar{1}1$ reflections, while for MgO(110) two sharper peaks, 180°-apart and centered at ψ~36.5°, arising from 111 and $\bar{1}11$ lattice planes, are visible. These peaks are positioned at identical ψ and ϕ values as the {111} peaks of their MgO substrates. This is illustrated in **Figure 3c** for the $Ta_{0.93}N$/MgO(001) film, where 111 XRD ϕ–scans, collected at a tilt angle of ψ = 54.74°, are plotted for both TaN layer and MgO substrate. This result shows that the film is epitaxial with a cube-on-cube relationship with the MgO substrate, [100] (001) $_{TaN}$ ‖ [100] (001) $_{MgO}$. The pole figure of the TaN/MgO(111) film displays one peak at the center (ψ=0°) and six peaks at ψ = 70.5°, separated by 60° in ϕ. The observed six-fold symmetry, instead of a threefold symmetry for a (111) cubic single-crystal, attests of the presence of two growth variants, rotated to each other by 180°, for the TaN/MgO(111) film. The origin of these two twin variants is yet to be explored. It can be possibly related to different nucleation of (111) planes at surface steps of the substrate, as observed previously for NbN epitaxial layers [70], or to the existence of stacking faults.

As judged from the XRD θ–2θ, ϕ-scans and pole figures, we conclude that all TaN_x films grow epitaxially with a cube-on-cube orientational relationship with respect to their MgO substrates, albeit that the TaN(111) film exhibits two growth variants.

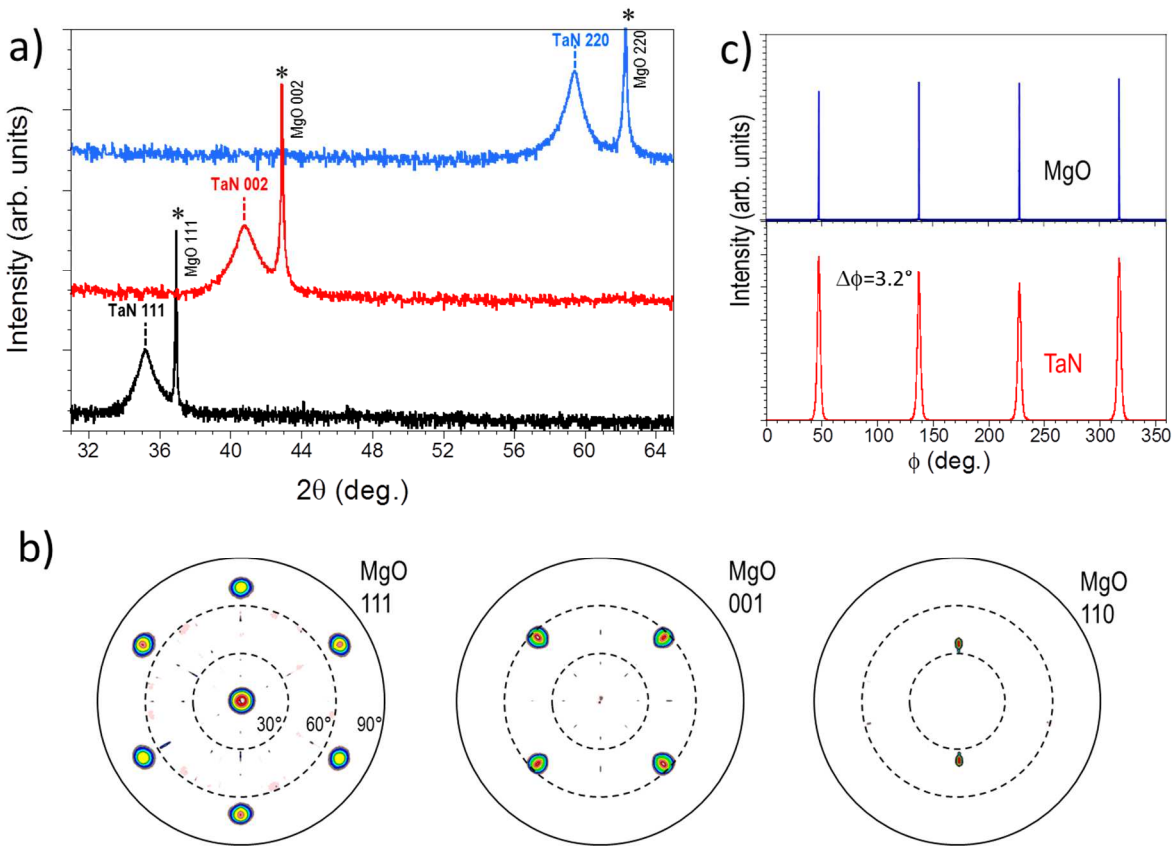

Figure 3: a) XRD θ–2θ scans and b) XRD {111} pole figures from TaN/MgO(111), $Ta_{0.93}N$/MgO(001) and $TaN_{0.99}$/MgO(110) sputter-deposited films. A representative {111} ϕ-scan (at ψ = 54.74°) is shown in c) for the $Ta_{0.93}N$/MgO(001) system, showing a cube-on-cube epitaxial growth of δ-TaN layer on MgO substrate.

The out-of-plane lattice constants, determined from the symmetric θ–2θ scans (**Fig. 3a**) are $a_{\perp}$= 4.410 Å, 4.414 Å and 4.397 Å, for TaN(111), $Ta_{0.93}N$(001) and $TaN_{0.99}$(110) films, respectively. These values correspond to a lattice mismatch along the growth direction in the range of 4.3–4.7% with respect to the MgO substrate (a_{MgO}=4.212 Å). Information on the relaxed (strain-free) lattice parameter, a_0, of the $Ta_{0.93}N$/MgO(001) film was obtained from XRD RSM around the asymmetric 113 reflection, as shown in **Figure 4**. The 113 peak of the TaN layer is extremely broad, located at $q_{\parallel}$= 0.331 ± 0.001 Å^{-1} and $q_{\perp}$= 0.677 ± 0.001 Å^{-1}, corresponding to in-plane lattice parameter $a_{\parallel}$ =4.27 ± 0.01 Å and out-of-plane lattice

parameter $a_\perp$= 4.429 ± 0.005 Å. This indicates the presence of compressive stress in this TaN layer. The stress-free lattice constant a_0 was determined from $a_\parallel$ and $a_\perp$ values through the relationship

$$a_0 = a_\perp \left(1 - \frac{2\nu}{1+\nu}\frac{a_\perp - a_\parallel}{a_\parallel}\right) \quad (9)$$

where $\nu = c_{12}/(c_{11}+c_{12})$ is the Poisson ratio of δ-TaN (001) film. Using a value of ν = 0.197 (as calculated from the measured single-crystal elastic constants of the $Ta_{0.93}N$/MgO(001) sample, see Section III.3 and supplementary material [52]), one obtains from Eq. (9) a_0 = 4.375 ± 0.01 Å. Shin *et al.* reported a slightly lower a_0 value of 4.351 Å for stoichiometric (x=1) δ-TaN_x (001) epitaxial layers deposited by reactive magnetron sputtering, but assuming a value of ν = 0.25 [33]. If we consider ν = 0.25 in Eq. (9), then one obtains a_0=4.36 Å, which is consistent within 0.3% to the value reported in Ref. [33]. Lower values of a_0 = 4.337 and 4.335 Å were reported for over-stoichiometric δ-$TaN_{1.17}$ and δ-$TaN_{1.22}$ films on MgO(001) [64,66]. For nitrogen-deficient films, contradictory values of a_0 = 4.330 Å and 4.355 Å were obtained for δ-$TaN_{0.95}$ [65] and δ-$TaN_{0.94}$ [66] layers epitaxially grown on Si(001) and MgO(001), respectively. Previous reports for polycrystalline δ-TaN_x films give a_0 between 4.33 and 4.44 Å [25,35,37,71–73], while the lattice constants for bulk cubic TaN powders range between 4.332 Å [74] and 4.340 Å (JCPDS File Card No. 49-1283).

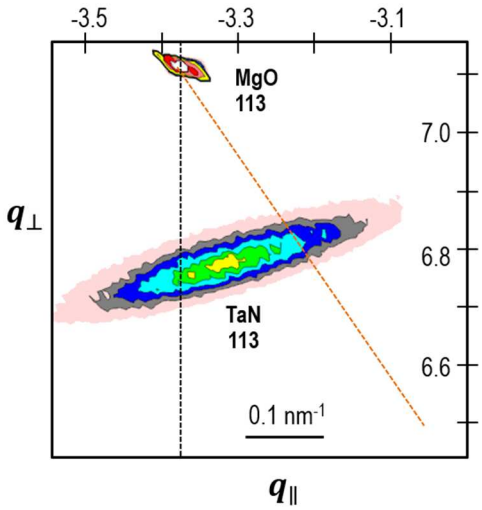

Figure 4: RSM around the 113 reflection of the $Ta_{0.93}N$/MgO(001) sample.

One can also notice from the RSM of **Fig. 4** that the 113 peak of the TaN(001) layer is not aligned with that of the MgO substrate along the $q_{\parallel}$ direction, evidencing for some in-plane strain relaxation. However, the film is not fully relaxed as its peak position does not lie on the dash-dotted line corresponding to $a_{\parallel} = a_{\perp} = a_{bulk}$. The degree of in-plane relaxation, defined as $R = (a_{\parallel} - a_{MgO})/(a_0 - a_{MgO})$, yields $R = 35\%$, corresponding to an in-plane compressive strain $\varepsilon_{\parallel} = (a_{\parallel} - a_0)/a_0$ of -2.41%. This compressive strain results primarily from differential thermal contraction upon cooling from deposition temperature (570°C) to RT, as well as incorporation in the TaN lattice of point defects due to the energetic particle bombardment of the growing film by heavy Ta sputtered atoms and backscattered Ar [75–77]. According to Balasubramanian *et al.* [42] stable point defects in δ-TaN_x compounds are predicted to be metal vacancy (T < 1500 K), nitrogen vacancy and nitrogen interstitial for N_2 vapor pressure of 1 Pa and a low defect concentration of 0.5 %. Entrapped Ar could also contribute to the observed increase in a_0, as also reported for cubic δ-$Ti_xTa_{1-x}N$ films [78].

The crystalline quality of the respective δ-TaN_x epitaxial films was assessed from the examination of the intensity profiles along the 2θ and ϕ directions. The out-of-plane X-ray coherence lengths, $\xi_{\perp}$, were determined from the width of the symmetric reflections shown in

Fig. 2a, according to $\xi_{\perp} = \frac{\lambda}{\Gamma_{2\theta}\cos\theta}$, where λ is the X-ray wavelength and $\Gamma_{2\theta}$ is the full width at half maximum (FWHM) peak intensity. Values of $\Gamma_{2\theta}$ = 0.53°, 0.71° and 0.42° were obtained for the TaN_x layers grown on MgO(111), MgO(001) and MgO(110) substrates, corresponding to $\xi_{\perp}$ = 18, 13 and 25 nm, respectively. These values are significantly lower that the value of 73 nm reported for stoichiometric δ-TaN films [66], which suggests globally a worse mosaicity along the growth direction, possibly due to smaller grains and/or higher degree of structural defects in our films as it will be shown later. However, the present value is consistent with that reported for $Ta_{0.94}N$ ($\xi_{\perp}$ = 34 nm) [66]. Note that in the study of Shin *et al*. [66] the highest crystalline quality ($\xi_{\perp}$ = 112 nm) was obtained for over-stoichiometric δ-TaN_x films with x between 1.13 and 1.22. For other group-5 binary TMNs, values of $\xi_{\perp}$ = 157 and 14 nm were reported for epitaxial VN (001) [69] and NbN_x (001) [79] films, respectively. The better crystalline quality of the $TaN_{0.99}$(110) film is confirmed from the lower FWHM value in ϕ-scans, Δϕ = 2.5°, in comparison with the other two orientations (Δϕ = 4.0° and 3.2° for TaN(111) and $Ta_{0.93}N$(001), respectively). This statement agrees with the analysis of their respective elastic properties, as discussed in Section 3.3.

3. 2. Phase stability and structural properties: DFT calculations

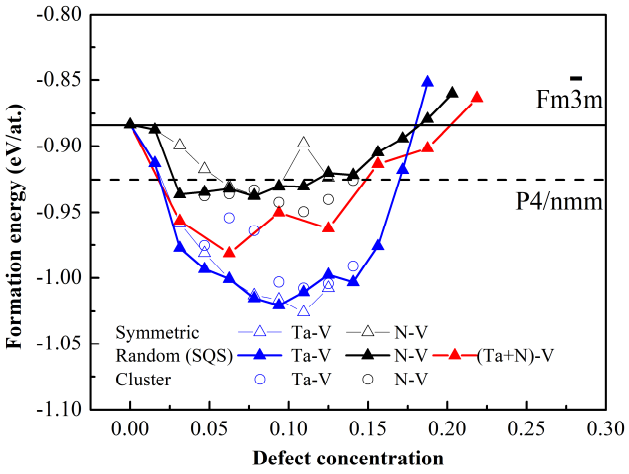

Figure 5: Formation energy in δ-TaN phase as a function of defect (Ta, N or (Ta+N) vacancy) concentration in supercell. Ordering/clustering configurations of atom species have been considered. The horizontal lines indicate the formation energy of the cubic $Fm\bar{3}m$ (solid line) and tetragonal P4/nmm (dashed-line) defect-free TaN structures. Not shown, the formation energy of the cubic NbO-type $Pm\bar{3}m$ simulating 25 at. % ordered Schottky defects is –0.727 eV/at., much higher than other compounds.

The calculated formation energy at 0 K of different defected and defect-free δ-TaN_x structures are shown in **Figure 5**. When we compare to the defect-free $Fm\bar{3}m$ cubic phase ($E_f = -0.884$ eV), the P4/nmm tetragonal phase is found to have a lower formation energy ($E_f = -0.925$ eV) and is thermodynamically, mechanically and dynamically stable, as previously established in the recent work of Hu *et al*. [80] and confirmed by the present calculations (see Suppl. Mat. [52]). From first-principles calculations, Hu *et al*. [80] concluded that the presence of point defects (Ta or N vacancies in low concentration, ~2%) or C or O impurities did not prevent the cubic to tetragonal phase transformation. Nonetheless, considering the small grain size of thin films (a few tens of nm) with low local coordinated sites on the surfaces or interfaces, they argued that such size effect could induce a stabilization of the TaN cubic phase, compared to its bulk counterpart. Many other non-stochiometric crystalline Ta_yN_x compounds were numerically investigated by Weinberger *et al*. [36] using first-principles methods but these authors did not discuss the case of the P4/nmm tetragonal phase.

From **Figure 5**, it is observed that the introduction of metal or nitrogen vacancies as well as Schottky defects stabilizes the cubic structure compared to the tetragonal one, for defect concentration in the 2.5-17.5 % range. The lowest formation energy of −1.02 eV is found for $Ta_{0.78}N$ (11 % Ta vacancy), as also predicted by Koutná *et al*. [41], whatever the defect configuration is. Nitrogen vacancies appear less energetically favourable than metal vacancies, whereas Schottky defects have intermediate formation energy between that of

metal and nitrogen vacancy, depending certainly on their configuration/interaction. One can notice that the formation energy of the cubic NbO-type ($Pm\bar{3}m$) simulating 25 at. % ordered Schottky defects is –0.727 eV/at., i.e., much higher than any other structures, indicating that such high amount of Schottky defects is not expected. The formation energy of one metal vacancy, one nitrogen vacancy and one Schottky-defect pair in δ-TaN is –3.345, +0.068, and –4.520 eV, respectively. These formation energies are in line with the values of –3.4 eV (Ta vacancy) and 0 eV (N vacancy) calculated by Balasubramanian *et al*. [42] if one considers the TaN reference state, instead. In agreement to previous calculations by Koutná *et al*. [41] our results also confirm that the configuration of defects does not play a significant role on the stabilization of both types of defects in this particular system, contrarily to MoN [41,81]. Moreover, the results on perfectly ordered Ta_yN_x compounds from CE method (see Suppl. Mat. [52]) or the "symmetric" cubic supercell reproduce well the variation of the formation energy with defect concentration obtained using a supercell with a "cluster" configuration or the SQS methodology with a random configuration (see Suppl. Mater. [52] for definition of supercells).

Our DFT calculations for δ-TaN_x compounds illustrate a monotonous decrease of the lattice parameter *a* from 4.426 to 4.305 Å as the vacancy concentration increases up to 20 % (see **Figure 6a**). The evolution of *a* appears sensitive to the type of defects, a stronger decrease being found for metal vacancies (blue symbols). Comparable trends were predicted previously from first-principles calculations by Stampfl and Freeman [82], Grumski *et al.* [83] and Koutná *et al*. [41]. **Figure 6a** additionally evidences a greater influence of defect configuration for metal vacancies, lower *a* values being obtained for ordered Ta vacancies ("symmetric" configuration, open blue triangles). It is also supported by the calculation of 25 at. % ordered Schottky defects simulated by the NbO-type structure, providing a lattice parameter as low as 4.252 Å [52]. It is even lower than the extrapolated one from SQS

randomly distributed Schottky defects. The sensitivity of the lattice constant to the type and defect concentration (> 2%) could explain the large spread of structural parameters reported in the literature.

When we compare in **Figure 6a** the experimental stress-free lattice parameter $a_0 = 4.375 \pm 0.01$ Å to the calculated a values of defected TaN_x structures, one should expect a maximum of ~6% ordered tantalum vacancy (open blue triangles) or ~11% random Schottky pair (red triangles) concentration to find a closer agreement between experimental and theoretical values. Taking into account the measured composition of the $Ta_{0.93}N$/MgO(001) sample, this would suggest the presence of ~3.5 % metal vacancy and ~8% Schottky defect concentration in this film. Note that the relative difference between the lattice constant values of the defect-free TaN compound and the defected $Ta_{0.93}N$(001) film is −1.2 %, corresponding to 3.6 % reduction in the unit cell-volume.

Following the approach of Koutná *et al*. [41] to provide a quantitative estimation of the lattice parameters, we fitted the calculated values for defect concentrations below 0.12, with linear functions of the defect concentration, x, (see **Figure 6a**):

$$a = a(0) - \beta x \qquad (10)$$

Here, $a(0)$ is the lattice parameter of defect-free δ-TaN (4.426 Å). Our fitted β values are 0.830, 0.338, and 0.480 Å for ordered (symmetric) Ta vacancies, random N vacancies and Schottky defects (Ta+N vacancies), respectively. They compare well to the previous values of 0.747, 0.358, and 0.573 Å reported by Koutná *et al*. [41]. In general, metal deficient Ta_xN structures show much greater volume decrease upon vacancy introduction than their nitrogen deficient counterparts. Similar trends have been reported by Gu *et al*. for δ-HfN_x compounds [84].

Interesting features are observed for the evolution of mass density with defect concentration: a significant decrease is found as the metal vacancy or the Schottky pair concentration increases, whereas the introduction of nitrogen vacancy leads to a slight

increase (see **Figure 6b**). One can also notice that the mass density is rather insensitive to the defect configuration. When we compare in **Figure 6b** the experimental mass density obtained from XRR ($\rho = 15.6 \pm 0.2$ g/cm^3) to the calculated values of defected δ-Ta_yN_x structures, one can easily observe that it lies outside the range of accessible values. It is ~4% higher than the mass density calculated for the defect-free δ-TaN structure (~15.0 g/cm^3) and ~10% higher than the value obtained considering a Schottky concentration of 10% (~14.0 g/cm^3). Part of the apparent underestimation of mass density from DFT calculations can be contributed to the overestimation of cell-volume by the GGA approximation (~3%). Also, the calculations do not consider the presence of entrapped Ar or cluster of interstitials. But experimentally, the impingement of energetic particles (sputtered Ta atoms and backscattered Ar) is known to cause film densification by incorporation of excess atoms at column boundaries, formation of interstitials (likely in the form of clusters) or entrapment of gas atoms. While the mass density measured from XRR corresponds to a *microscopic average*, including both column boundary regions and diffracting domains, the DFT calculations solely mimic the crystal part (i.e., *intrinsic* mass density). We believe this different probing scale to be at the origin of the observed discrepancy.

The mass density at the crystal scale can be estimated from XRD data [85]. Considering the previous defect concentration inferred in the $Ta_{0.93}N$/MgO(001) sample yields a value of $\rho_{XRD} \sim 13.7 \pm 0.5$ g/cm^3 (solid line), consistent with DFT calculations. This is a reduction of ~12 % respectively to ρ_{XRR} value. It means that in the present case, the *intrinsic* mass density has to be evaluated from the volume of the fcc lattice $(a_0)^3$ and the total mass (m) considering ~3.5 % Ta vacancy and ~8 % Schottky pair.

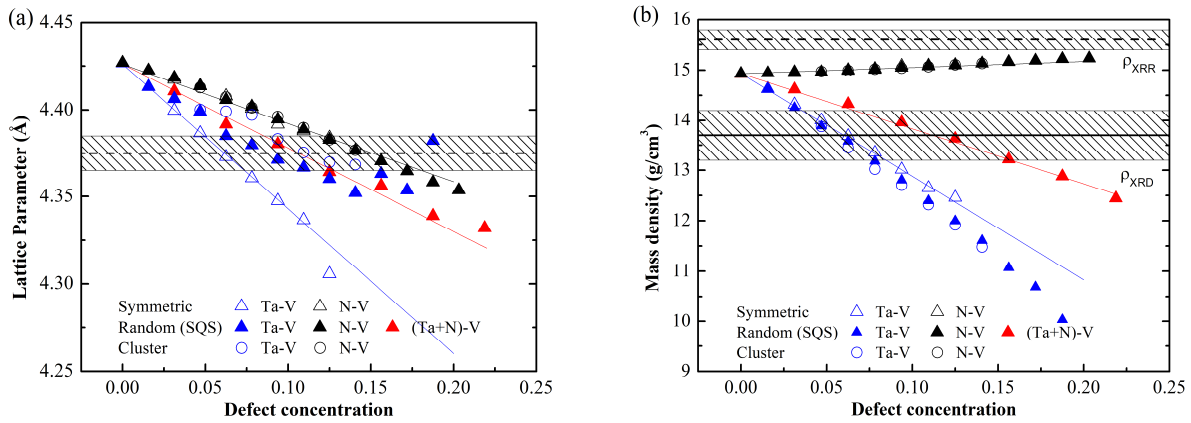

Figure 6: Calculated (a) equilibrium lattice parameter and (b) mass density as a function of defect (Ta, N or (Ta+N) vacancy) concentration in δ-TaN structures. The solid lines are linear fit to the data for vacancy concentration below 12 % according to Eq. (10). The horizontal lines indicate our experimental data obtained from XRD (a_0 = 4.375 ± 0.01 Å and ρ_{XRD} = 13.7 ± 0.5 g/cm^3 for the defected structure) and XRR (ρ_{XRR} = 15.6 ± 0.2 g/cm^3). Error bars to experimental data are shown as dashed regions.

3.3. Sound velocities and elastic constants

The vertical longitudinal sound velocity V_L [001] of bulk wave propagating along the growth direction [001] and the transverse sound velocity V_T [100] propagating along the in-plane [100] direction of the $Ta_{0.93}N$/MgO(001) sample have been selectively measured by the PLU and BLS techniques, respectively (see **Figs. S1** and **S2** [52]). This provides a selective measurement of c_{11} and c_{44} single-crystal elastic constants. The remaining independent elastic constant, namely c_{12}, has been determined by the fitting of several BLS spectra obtained at different angles of incidence (see **Fig. S2**. [52]). It enables the calculation of the Poisson ratio $\nu = c_{12}/(c_{11}+c_{12})$ = 0.197. Additionally, vertical longitudinal sound velocity V_L [011] and V_L [111] of bulk wave propagating along the [011] and [111] growth directions of the $TaN_{0.99}$/MgO(110) and TaN/MgO(111) samples, respectively, have been selectively measured

by PLU (see **Fig. S1**). The measured sound velocities and elastic constants are reported in **Table S1** [52].

The obtained experimental single-crystal elastic constants from the $Ta_{0.93}N$/MgO(001) sample are the following: c_{11} = 530 ± 10 GPa, c_{12} = 130 ± 5 GPa and c_{44} = 137 ± 3 GPa. This yields a Zener anisotropy ratio $A = 2c_{44}/(c_{11} - c_{12})$ equal to 0.685. This value is significantly larger than the value of A = 0.16 predicted by DFT calculations for the perfect δ-TaN compound. However, both A values are <1, signifying that the elastically stiffest direction is along [001] for δ-TaN compound. This is reflected also by the fact that V_L[001] > V_L[011] > V_L[111]. Note that the calculated V_L[011] and V_L[111] velocities (5471 and 5347 m/s, respectively) from the $Ta_{0.93}N$/MgO(001) sample slightly differ from the ones (5656 and 5635 m/s, respectively) measured directly on the $TaN_{0.99}$/MgO(110) and TaN/MgO(111) samples (compare solid and dashed lines in **Fig.7c-d**) but remain below V_L[001] (5830 m/s). This is contributed to different film compositions, associated with different point defect concentrations (see below), depending on crystal growth orientation despite the films being deposited in the same batch. Variations in the metal/nitrogen ratio and electrical resistivity were also reported by Oszdolay *et al*. [86,87] in sputter-deposited WN_x epitaxial layers for which the only difference was the substrate type or orientation.

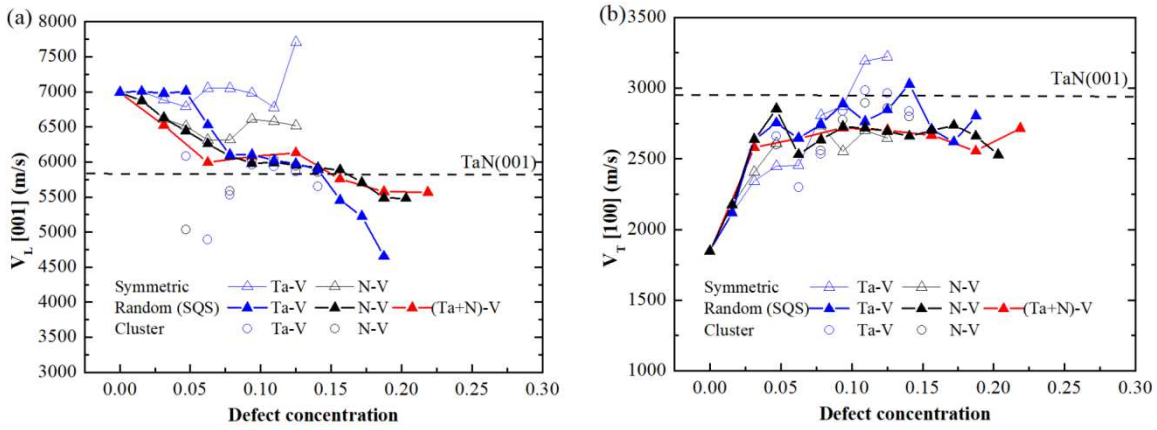

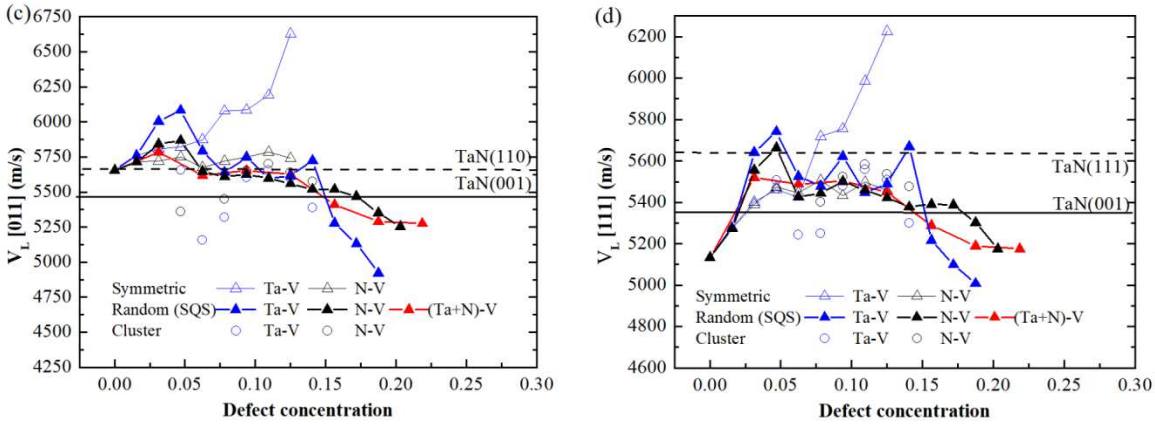

Figure 7: Calculated sound velocities as a function of defect (Ta, N or (Ta+N) vacancy) concentration in δ-TaN structures. (a) V_L [001], (b) V_T [100], (c) V_L [011], (d) V_L [111]. The horizontal dashed-lines indicate our experimental data selectively measured by PLU and BLS (a-b) on the $Ta_{0.93}N$/MgO(001) film and PLU (c-d) on $TaN_{0.99}$/MgO(011) and TaN/MgO(111) films, respectively. In (c-d) the solid line is calculated from experimental c_{ij}'s of the $Ta_{0.93}N$/MgO(001) sample.

Comparisons of DFT calculations considering defected δ-TaN_x structures and experimental results are collected in **Figure 7** for V_L and V_T. All sound velocities show different trends with increasing defect concentration and configuration type. If we restrict the discussion to Schottky-type defects, one can see that V_L [001] is decreasing, while V_T [100] and V_L [111] are first increasing until a plateau is reached. For the specific (110) crystal orientation, Schottky defects have surprisingly no noticeable influence on the longitudinal sound velocity until ~15 % defect concentration, with V_L [011] being equal to ~5625 m/s. This value agrees with the experimental value of 5656 m/s of the $TaN_{0.99}$/MgO(110) sample; however, a stiffening of V_L[011] is predicted when considering metal vacancies, especially for "symmetric" configuration up to ~12%. Nevertheless, for the two other crystal orientations, the predicted trends provide a mean to estimate the influence of the defect concentration on the elastic response of TaN_x compounds.

Measured V_L [001] (5830 m/s) and V_T [100] (2963 m/s) are 20% lower and 76 % higher than the defect-free calculated values, 6994 and 1848 m/s, respectively (see **Table S2** [52]). Interestingly, considering the presence of metal or nitrogen vacancies allows explaining these huge discrepancies, see **Figures 7a** and **7b**. At least 7 % up to 15 % Schottky defects have to be considered to match the experimental V_L [001] value of the $Ta_{0.93}N$/MgO(001) sample. This range of defect concentration is consistent with the previous discussion on the structural parameters (a_0 and ρ), see **Figure 6**. It is also remarkable that it corresponds to the lowest formation energy of the defected δ-TaN_x structure, see **Figure 5**. For V_T [100], accounting for Ta vacancies in addition to Schottky defects would enable to reach the experimental value above the "plateau". A lower defect concentration is expected, from 2.5% up to 12 % Schottky defects, for the TaN/MgO(111) sample.

Figure 8 displays the evolutions of the computed single-crystal elastic constants, c_{11}, c_{12} and c_{44}, as well as a combination of these data, as a function of defect concentration, and their comparison with experimental data. c_{11} and B have the same decreasing trend as defect concentration is increasing, pointing towards a more compliant material (see **Figure 8a** and **8c**, respectively). The experimental values, $c_{11} = 530$ GPa and $B = 263$ GPa, are ~20-27% lower than the calculated values of defect-free TaN compound, $c_{11} = 731$ GPa and $B = 325$ GPa (see **Table S2** [52]). One has to consider the presence of 10-15% vacancies (Ta vacancies and/or Schottky pairs) to obtain a satisfying agreement with experimental data, in agreement with the previous estimations for lattice parameter (mixing of 3.5 % Ta vacancy and 8 % Schottky). On the other hand, a stiffening of the c_{44} elastic constant is observed with defect incorporation and the value saturates around 100 ± 15 GPa for defect concentration >5%, see **Fig. 8d**. The experimental value, c_{44} = 137 GPa, is ~180% higher than the computed value of 50 GPa of the defect-free TaN compound, but could be approached by considering at least 11% defect concentration. Note that a value of 122 GPa is derived for c_{44} if one considers ρ_{XRD} instead of ρ_{XRR}. Similarly, the c_{12} elastic constant is found to first increase and

then remains practically constant with introduction of defects, see **Fig. 8b**, although its variations are less pronounced than for c_{44}. The present DFT calculations demonstrate that introduction of vacancy-type defects into δ-TaN structure in concentration up to ~10% leads to a more compliant (from B = 325 to ~280 GPa) and less anisotropic (from A = 0.16 to 0.55) material. Electronic structure calculations (not reported here) of density of states (DOS) show that the presence of vacancies in TaN_x structures leads to a reduced number of *p-d* bonding states (integrated in the −10 to −4 eV interval), which weakens the bond strength, and could explain the observed c_{11} softening. The DOS at the Fermi level, corresponding to *d-d* metallic bonding states, is also reduced with introduction of either metal or nitrogen vacancy with respect to perfect δ-TaN, likely at the origin of c_{44} stiffening [15,18]. Similar trends were reported by Jhi *et al*. [88] in sub-stoichiometric NbC_x compounds (same group-5 metal).

The value of 502 GPa, as measured by PLU for the modulus $(c_{11}+c_{12}+2c_{44})/2$, along the [110] direction of the $TaN_{0.99}$/MgO(110) sample, compares well to the calculated values of defected structures over a wide range of concentration, see **Figure 8e**. While Ta vacancies and Schottky defects tend to decrease $(c_{11}+c_{12}+2c_{44})/2$ for concentrations larger than 5%, this modulus is found to be rather insensitive to N vacancy concentration, having a value of 480 ± 20 GPa for nitrogen deficient structures with concentration up to 15%. Although it is unrealistic to predict from the trends shown in **Fig. 8e** which defect concentration would match at best the experimental $(c_{11}+c_{12}+2c_{44})/2$ value, the findings do not contradict the earlier statement that the $TaN_{0.99}$/MgO(110) film showed the best crystalline quality and is stoichiometric.

For $(c_{11}+2c_{12}+4c_{44})/3$, an increase from 395 to 460-480 GPa is noticed with increasing defect concentration up to 5%, followed by a substantial softening for higher defect concentrations, see **Fig. 8f**. The value of 498 GPa, as measured along the [111] direction of the TaN/MgO(111) sample by PLU, would be approached by considering a defect concentration of at least 5%. Schottky defects alone could not provide a closer agreement as

for the (001)-oriented TaN film, which may indicate that this film is not stoichiometric. The relative difference between the defect-free and the defected film (minimum 5 % defect concentration) is −25%.

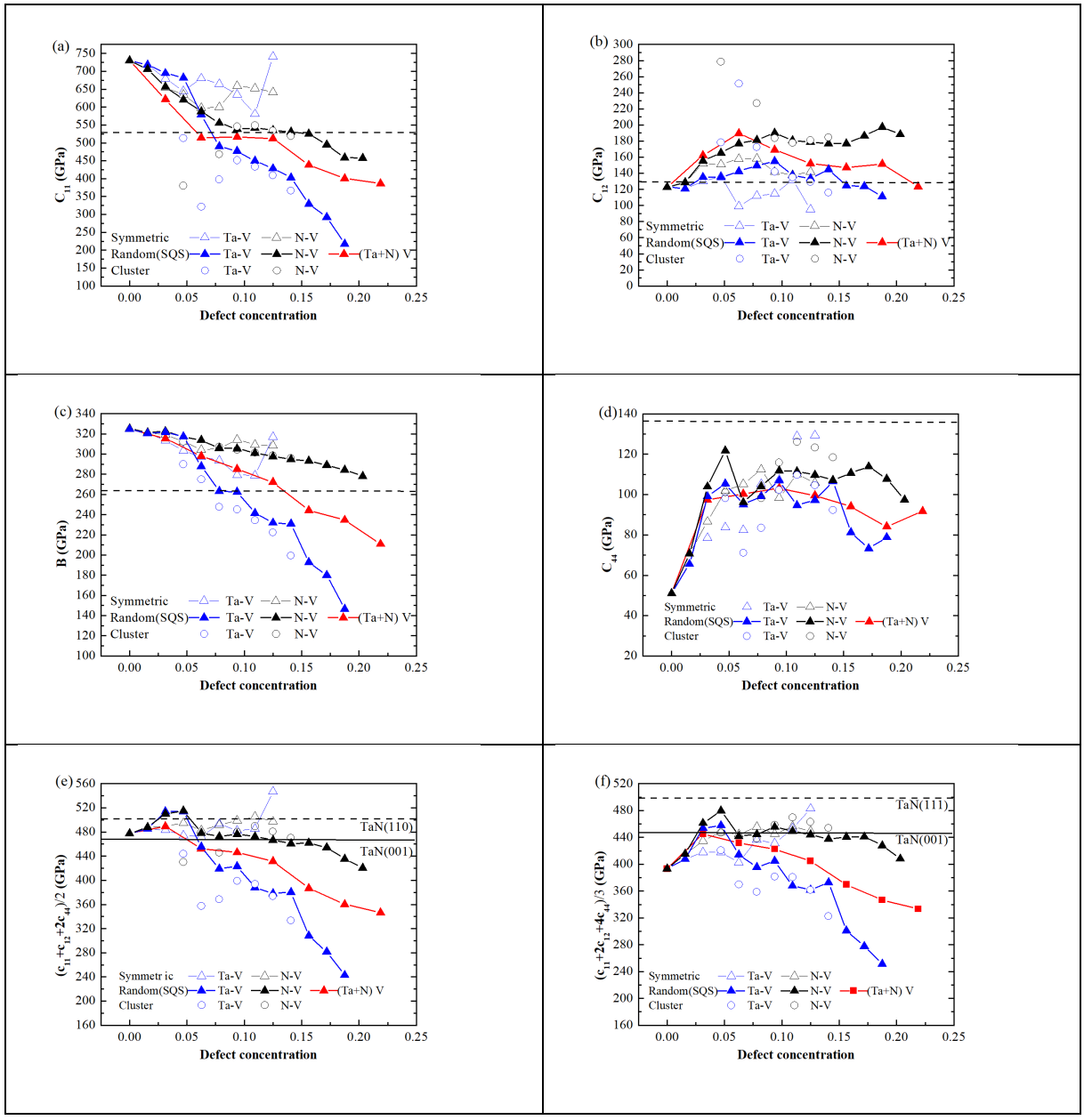

Figure 8: Calculated elastic constants as a function of defect (Ta, N or (Ta+N) vacancy) concentration in δ-TaN structures. (a) c_{11}, (b) c_{12}, (c) $B = (c_{11}+2c_{12})/3$, (d) c_{44}, (e) $(c_{11}+c_{12}+2c_{44})/2$ and (f) $(c_{11}+2c_{12}+4c_{44})/3$. The dashed-line indicates our experimental data selectively measured by BLS (b-d) and PLU (a) on the $Ta_{0.93}N$/MgO(001) film, and by PLU (e-f) on $TaN_{0.99}$/MgO(110) and TaN/MgO(111) films, respectively. In (e-f) the solid line is calculated from experimental c_{ij}'s of the $Ta_{0.93}N$/MgO(001) sample.

As energetics of cubic and tetragonal structures may remain very close for small amounts of defect (< 2.5%), we should compare the elastic properties of the defected $Fm\bar{3}m$ cubic structure and of the defect-free P4/nmm tetragonal phase. As presented in **Table S2** of the Suppl. Mat. [52] and in Ref. [80], the elastic properties of P4/nmm(I) are closed to the ones of P4/nmm. Whereas the c_{44} elastic constant (120 GPa) is comparable to our experimental value (137 GPa), the c_{33} elastic constant (262 GPa) is very different from both that of defect-free δ-TaN (731 GPa) and experimental value (530 GPa). This rules out the possible stabilization of a tetragonal structure in our as-deposited TaN films [89] and further suggests that the cubic phase contains a defect concentration higher than 2.5 %.

3.4. Static and dynamical mechanical stability

There are three independent elastic constants in a solid crystal with cubic symmetry: c_{11}, c_{12}, and c_{44}. With no external stresses applied, its static mechanical stability requires that $c_{44} > 0$, $c' = (c_{11}-c_{12})/2 > 0$, and $B = (c_{11}+2c_{12})/3 > 0$ [90]. This first static criterion is easily verified and the present findings confirm that as-deposited TaN films are mechanically stable. The same holds for the calculated δ-TaN structures as well as ordered TaN_x ($x \leqslant 1$) and Ta_xN ($x \leqslant 1$) compounds computed by CE (see **Tables S2** and **S4** [52]). The second criterion concerns the dynamical mechanical stability that can be inferred from vibrations calculations. The phonon dispersion properties of several ordered structures (defect-free $Fm\bar{3}m$ and P4/nmm TaN, Ta_3N_4 and Ta_4N_3 compounds with $Pm\bar{3}m$ structure having 12.5 % Ta and N vacancy concentration, see **Table S6** [52]) were calculated by PHONONPY code [91] within the harmonic approximation, using density functional perturbation theory (DFPT) calculations implemented in VASP [46,47]. Details of the calculations and results are reported in Suppl. Mat. [52].

The imaginary frequencies indicate dynamic instability for defect-free δ-TaN (see **Fig. S4**), while P4/nmm TaN is thermodynamically more stable (as already discussed, see **Fig. 5**) and dynamically stable (see **Fig. S5**). At low vacancy concentrations (< 2.5 %, see **Fig. 5**), the cubic structure is still energetically not favourable and could easily transform to the more dynamically stable tetragonal phase after atomic relaxation [80]. However, for much higher defect concentration, defected δ-TaN structures become energetically more stable, similarly to the ordered defected structures with 12.5% Ta or N vacancy concentration. The phonon calculations on these two phases (see **Figs. S6** and **S7**) show that imaginary frequencies were not totally vanished though but can be suppressed by introducing more vacancies and/or ordering configuration. This suggests that vacancies, known as cubic TaN phase-stabilizer from energetics, can indeed decrease the dynamic instability as well.

4. Summary and conclusions

A comprehensive study on the structure and elastic properties of cubic TaN system has been carried out combining thin film growth experiments and first-principles calculations. Single-crystal TaN films with cubic rocksalt structure and different crystal orientations -(001), (110) and (111)- have been epitaxially grown at 570°C on MgO substrates by reactive magnetron sputtering. The combination of the BLS and PLU techniques enables us to determine the complete set of elastic constants for the δ-$Ta_{0.93}N$ film with (001) orientation, namely c_{11} = 530 GPa, c_{12} = 130 GPa and c_{44}=137 GPa. Although the Ta:N ratio was close to the 1:1 stoichiometry, the confrontation of experimental findings on structural and elastic properties of these films to calculations advocates for the presence of ~10-15% Schottky-type defects in the as-deposited films. Notably, this range of defect concentration corresponds to local minima of the formation energy for the cubic defected δ-TaN structure observed at ~11% vacancy concentration, with Ta vacancies being the more energetically favoured point defects at 0 K.

The trends revealed by the present computation of the elastic constants of defected TaN_x structures clearly demonstrate a significant influence of metal and nitrogen vacancy concentration on the elasticity of the TaN system. Overall, the type of defect configuration - random distribution versus ordering/clustering- has a marginal impact on the observed variations. Introduction of vacancies at either metal, nitrogen or both sub-lattices in δ-TaN leads to a more compliant and less anisotropic material. The largest deviation (+180%) between the defect-free and the defected $Ta_{0.93}N$ film with ~11% defect concentration is observed for the c_{44} elastic constant. This can provide explanation for the large scatter of shear elastic modulus values reported in literature depending on the working pressure. For c_{11} and *B*, we find a relative difference of −27 % and −19 %, respectively, between experimental data and calculated values for defect-free δ-TaN.

Calculated $(c_{11}+2c_{12}+4c_{44})/3$ has an increasing trend as defect concentration is increasing until ~5 % and then is decreasing. It compares reasonably well to the value measured along the TaN[111] direction of the TaN/MgO(111) sample by PLU considering at least 5% of Schottky defects and likely additional metal vacancies. $(c_{11}+c_{12}+2c_{44})/2$ measured by PLU along the [110] direction of the $TaN_{0.99}$/MgO(110) sample with best crystalline quality compares well to the calculated values for tantalum vacancy and Schottky defects in a broad range of defect concentration (0-12 %).

These elastic constants and moduli can be used to probe the defect concentration introduced in TaN thin films as a function of the growth conditions (temperature and N_2 partial pressure) and crystal orientation. The present findings also reveal that TaN layers with different orientations, as a result of epitaxial growth on different substrates, may have different *intrinsic* elastic and electrical properties due to different point defect concentration. The overall results of this work attest of the decisive role of point defects in controlling

structural and elastic properties of transition metal nitrides, and their tailoring is likely to result in further beneficial improvement of their performances.

Acknowledgements:

This work has been performed within the M.ERA-NET project MC^2 "Multi-scale Computational-driven design of novel hard nanostructured Coatings" and funded by the French ANR program (Project No. ANR-13-MERA-0002-02). C-H. Li acknowledge the support of CSC for his PhD funding. Q-M. Hu acknowledge the support of university Paris 13 for several visiting professor positions.

References

[1] P. Patsalas, N. Kalfagiannis, S. Kassavetis, G. Abadias, D.V. Bellas, C. Lekka, E. Lidorikis, Conductive nitrides: Growth principles, optical and electronic properties, and their perspectives in photonics and plasmonics, Mater. Sci. Eng. R Reports. 123 (2018) 1–55. doi:10.1016/j.mser.2017.11.001.

[2] G. Abadias, V.I. Ivashchenko, L. Belliard, P. Djemia, Structure, phase stability and elastic properties in the Ti1-xZrxN thin-film system: Experimental and computational studies, Acta Mater. 60 (2012) 5601–5614. doi:10.1016/j.actamat.2012.07.014.

[3] J.E. Sundgren, Structure and Properties of TiN coatings, Thin Solid Films. 128 (1985) 21–44.

[4] A. Hörling, L. Hultman, M. Odén, J. Sjölén, L. Karlsson, Mechanical properties and machining performance of Ti1−xAlxN-coated cutting tools, Surf. Coatings Technol. 191 (2005) 384–392. doi:10.1016/j.surfcoat.2004.04.056.

[5] G.M. Matenoglou, L.E. Koutsokeras, P. Patsalas, Plasma energy and work function of conducting transition metal nitrides for electronic applications, Appl. Phys. Lett. 94 (2009) 152108. doi:10.1063/1.3119694.

[6] C. Metaxa, S. Kassavetis, J.F. Pierson, D. Gall, P. Patsalas, Infrared Plasmonics with Conductive Ternary Nitrides, ACS Appl. Mater. Interfaces. 9 (2017) 10825–10834. doi:10.1021/acsami.6b16343.

[7] P. Patsalas, N. Kalfagiannis, S. Kassavetis, Optical properties and plasmonic performance of titanium nitride, Materials (Basel). 8 (2015) 3128–3154. doi:10.3390/ma8063128.

[8] S. Kassavetis, D.V. V. Bellas, G. Abadias, E. Lidorikis, P. Patsalas, Plasmonic spectral tunability of conductive ternary nitrides, Appl. Phys. Lett. 108 (2016) 263110. doi:10.1063/1.4955032.

[9] A. Le Febvrier, N. Van Nong, G. Abadias, P. Eklund, P-type Al-doped Cr-deficient CrN thin films for thermoelectrics, Appl. Phys. Express. 11 (2018) 051003. doi:10.7567/APEX.11.051003.

[10] S. Kerdsongpanya, O. Hellman, B. Sun, Y.K. Koh, J. Lu, N. Van Nong, S.I. Simak, B. Alling, P. Eklund, Phonon thermal conductivity of scandium nitride for thermoelectrics from first-principles calculations and thin-film growth, Phys. Rev. B. 96 (2017) 195417. doi:10.1103/PhysRevB.96.195417.

[11] C.X. Quintela, J.P. Podkaminer, M.N. Luckyanova, T.R. Paudel, E.L. Thies, D.A. Hillsberry, D.A. Tenne, E.Y. Tsymbal, G. Chen, C.B. Eom, F. Rivadulla, Epitaxial

CrN Thin films with high thermoelectric figure of merit, Adv. Mater. 27 (2015) 3032–3037. doi:10.1002/adma.201500110.

[12] Y. Zhong, X. Xia, F. Shi, J. Zhan, J. Tu, H.J. Fan, Transition Metal Carbides and Nitrides in Energy Storage and Conversion, Adv. Sci. 3 (2016) 1500286. doi:10.1002/advs.201500286.

[13] Z. Qi, B. Wei, J. Wang, Y. Yang, Z. Wang, Nanostructured porous CrN thin films by oblique angle magnetron sputtering for symmetric supercapacitors, J. Alloys Compd. 806 (2019) 953–959. doi:10.1016/j.jallcom.2019.07.325.

[14] D. Holec, M. Friák, J. Neugebauer, P.H. Mayrhofer, Trends in the elastic response of binary early transition metal nitrides, Phys. Rev. B. 85 (2012) 064101. doi:10.1103/PhysRevB.85.064101.

[15] D.G. Sangiovanni, L. Hultman, V. Chirita, Supertoughening in B1 transition metal nitride alloys by increased valence electron concentration, Acta Mater. 59 (2011) 2121–2134. doi:10.1016/j.actamat.2010.12.013.

[16] H. Kindlund, D.G. Sangiovanni, J. Lu, J. Jensen, V. Chirita, I. Petrov, J.E. Greene, L. Hultman, Effect of WN content on toughness enhancement in $V_{1-x}W_xN$/MgO(001) thin films, J. Vac. Sci. Technol. A Vacuum, Surfaces, Film. 32 (2014) 030603. doi:10.1116/1.4867610.

[17] H. Kindlund, G. Greczynski, E. Broitman, L. Martínez-de-Olcoz, J. Lu, J. Jensen, I. Petrov, J.E. Greene, J. Birch, L. Hultman, V0.5Mo0.5Nx/MgO(001): Composition, nanostructure, and mechanical properties as a function of film growth temperature, Acta Mater. 126 (2017) 194–201. doi:10.1016/j.actamat.2016.12.048.

[18] D.G. Sangiovanni, Inherent toughness and fracture mechanisms of refractory transition-metal nitrides via density-functional molecular dynamics, Acta Mater. 151 (2018) 11–20. doi:10.1016/j.actamat.2018.03.038.

[19] D.G. Sangiovanni, L. Hultman, V. Chirita, I. Petrov, J.E. Greene, Effects of phase stability, lattice ordering, and electron density on plastic deformation in cubic TiWN pseudobinary transition-metal nitride alloys, Acta Mater. 103 (2016) 823–835. doi:10.1016/j.actamat.2015.10.039.

[20] H. Kindlund, D.G. Sangiovanni, J. Lu, J. Jensen, V. Chirita, J. Birch, I. Petrov, J.E. Greene, L. Hultman, Vacancy-induced toughening in hard single-crystal V0.5Mo0.5Nx/MgO(001) thin films, Acta Mater. 77 (2014) 394–400. doi:10.1016/j.actamat.2014.06.025.

[21] L. Zhou, D. Holec, P.H. Mayrhofer, Ab initio study of the alloying effect of transition

metals on structure, stability and ductility of CrN, J. Phys. D. Appl. Phys. 46 (2013) 365301. doi:10.1088/0022-3727/46/36/365301.

[22] D. Holec, L. Zhou, R. Rachbauer, P.H. Mayrhofer, Alloying-related trends from first principles: An application to the Ti-Al-X-N system, J. Appl. Phys. 113 (2013) 113510. doi:10.1063/1.4795590.

[23] V. Petrman, J. Houska, Trends in formation energies and elastic moduli of ternary and quaternary transition metal nitrides, J. Mater. Sci. 48 (2013) 7642–7651. doi:10.1007/s10853-013-7582-4.

[24] G. Abadias, M.B. Kanoun, S. Goumri-Said, L. Koutsokeras, S.N. Dub, P. Djemia, Electronic structure and mechanical properties of ternary ZrTaN alloys studied by ab initio calculations and thin-film growth experiments, Phys. Rev. B. 90 (2014) 144107. doi:10.1103/PhysRevB.90.144107.

[25] G. Abadias, P. Djemia, L. Belliard, Alloying effects on the structure and elastic properties of hard coatings based on ternary transition metal (M=Ti, Zr or Ta) nitrides, Surf. Coatings Technol. 257 (2014) 129–137.

[26] F. Wang, D. Holec, M. Odén, F. Mücklich, I.A. Abrikosov, F. Tasnádi, Systematic ab initio investigation of the elastic modulus in quaternary transition metal nitride alloys and their coherent multilayers, Acta Mater. 127 (2017) 124–132. doi:10.1016/j.actamat.2017.01.017.

[27] F.F. Klimashin, P.H. Mayrhofer, Ab initio-guided development of super-hard Mo–Al–Cr–N coatings, Scr. Mater. 140 (2017) 27–30. doi:10.1016/j.scriptamat.2017.06.052.

[28] L. Zhou, F.F. Klimashin, D. Holec, P.H. Mayrhofer, Structural and mechanical properties of nitrogen-deficient cubic Cr–Mo–N and Cr–W–N systems, Scr. Mater. 123 (2016) 34–37. doi:10.1016/j.scriptamat.2016.05.036.

[29] J. Buchinger, N. Koutná, Z. Chen, Z. Zhang, P.H. Mayrhofer, D. Holec, M. Bartosik, Toughness enhancement in TiN/WN superlattice thin films, Acta Mater. 172 (2019) 18–29. doi:10.1016/j.actamat.2019.04.028.

[30] P. Řehák, M. Černý, D. Holec, Interface-induced electronic structure toughening of nitride superlattices, Surf. Coatings Technol. 325 (2017) 410–416. doi:10.1016/j.surfcoat.2017.06.065.

[31] K. Balasubramanian, S. V. Khare, D. Gall, Valence electron concentration as an indicator for mechanical properties in rocksalt structure nitrides, carbides and carbonitrides, Acta Mater. 152 (2018) 175–185. doi:10.1016/j.actamat.2018.04.033.

[32] H. Kindlund, D.G. Sangiovanni, L. Martínez-De-Olcoz, J. Lu, J. Jensen, J. Birch, I.

Petrov, J.E. Greene, V. Chirita, L. Hultman, Toughness enhancement in hard ceramic thin films by alloy design, APL Mater. 1 (2013) 042104. doi:10.1063/1.4822440.

[33] C.-S. Shin, Y.-W. Kim, N. Hellgren, D. Gall, I. Petrov, J.E. Greene, Epitaxial growth of metastable δ-TaN layers on MgO(001) using low-energy, high-flux ion irradiation during ultrahigh vacuum reactive magnetron sputtering, J. Vac. Sci. Technol. A Vacuum, Surfaces, Film. 20 (2002) 2007–2017. doi:10.1116/1.1513639.

[34] A.B. Mei, B.M. Howe, C. Zhang, M. Sardela, J.N. Eckstein, L. Hultman, A. Rockett, I. Petrov, J.E. Greene, Physical properties of epitaxial ZrN/MgO(001) layers grown by reactive magnetron sputtering, J. Vac. Sci. Technol. A Vacuum, Surfaces, Film. 31 (2013) 061516. doi:10.1116/1.4825349.

[35] P. Djemia, M. Benhamida, K. Bouamama, L. Belliard, D. Faurie, G. Abadias, Structural and elastic properties of ternary metal nitrides TixTa1−xN alloys : First-principles calculations versus experiments, Surf. Coat. Technol. 215 (2013) 199–208. doi:10.1016/j.surfcoat.2012.09.059.

[36] C.R. Weinberger, X.X. Yu, H. Yu, G.B. Thompson, Ab initio investigations of the phase stability in group IVB and VB transition metal nitrides, Comput. Mater. Sci. 138 (2017) 333–345. doi:10.1016/j.commatsci.2017.07.005.

[37] C.-S. Shin, Y.-W. Kim, D. Gall, J.E. Greene, I. Petrov, Phase composition and microstructure of polycrystalline and epitaxial TaNx layers grown on oxidized Si(001) and MgO(001) by reactive magnetron sputter deposition, Thin Solid Films. 402 (2002) 172–182. doi:10.1016/S0040-6090(01)01618-2.

[38] T.E. Kim, S. Han, W. joon Son, E. Cho, H.S. Ahn, S. Shin, Phase stability and electronic structures of stoichiometric tantalum mononitrides, Comput. Mater. Sci. 44 (2008) 577–580. doi:10.1016/j.commatsci.2008.04.017.

[39] A.N. Christensen, B. Lebech, A reinvestigation of the structure of ε-tantalum nitride, Acta Crystallogr. Sect. B Struct. Sci. 34 (1978) 261–263. doi:10.1107/S0567740878002733.

[40] A. V. Tsvyashchenko, S. V. Popova, E.S. Alekseev, Band Structure of Hexagonal Tantalum Nitride, Phys. Status Solidi. 100 (1980) 99–102. doi:10.1002/pssb.2221000109.

[41] N. Koutná, D. Holec, O. Svoboda, F.F. Klimashin, P.H. Mayrhofer, Point defects stabilise cubic Mo-N and Ta-N, J. Phys. D. Appl. Phys. 49 (2016) 375303. doi:10.1088/0022-3727/49/37/375303.

[42] K. Balasubramanian, S. V. Khare, D. Gall, Energetics of point defects in rocksalt

structure transition metal nitrides: thermodynamic reasons for deviations from stoichiometry, Acta Mater. 159 (2018) 77–88. doi:10.1016/j.actamat.2018.07.074.

[43] N. Koutná, D. Holec, M. Friák, P.H. Mayrhofer, M. Šob, Stability and elasticity of metastable solid solutions and superlattices in the MoN–TaN system: First-principles calculations, Mater. Des. 144 (2018) 310–322. doi:10.1016/j.matdes.2018.02.033.

[44] G. Abadias, L.E. Koutsokeras, S.N. Dub, G.N. Tolmachova, A. Debelle, T. Sauvage, P. Villechaise, Reactive magnetron cosputtering of hard and conductive ternary nitride thin films: Ti-Zr-N and Ti-Ta-N, J. Vac. Sci. Technol. A. 28 (2010) 541–551. doi:10.1116/1.3426296.

[45] L.G. Parratt, Surface Studies of Solids by Total Reflection of X-Rays, Phys. Rev. 95 (1954) 359–369.

[46] G. Kresse, J. Furthmüller, Efficient iterative schemes for ab initio total-energy calculations using a plane-wave basis set, Phys. Rev. B. 54 (1996) 11169–11186.

[47] G. Kresse, From ultrasoft pseudopotentials to the projector augmented-wave method, Phys. Rev. B. 59 (1999) 1758–1775.

[48] W. Kohn, L.J. Sham, Self-consistent equations including exchange and correlation effects, Phys. Rev. (1965) A1133–A1138.

[49] J.P. Perdew, K. Burke, M. Ernzerhof, Generalized Gradient Approximation Made Simple, Phys. Rev. Lett. 77 (1996) 3865–3868.

[50] A. Zunger, S.-H. Wei, L.G. Ferreira, J.E. Bernard, Special quasirandom structures, Phys. Rev. Lett. 65 (1990) 353–356. doi:10.1103/PhysRevLett.65.353.

[51] D. Lerch, O. Wieckhorst, G.L.W. Hart, R.W. Forcade, S. Müller, UNCLE: A code for constructing cluster expansions for arbitrary lattices with minimal user-input, Model. Simul. Mater. Sci. Eng. 17 (2009) 055003. doi:10.1088/0965-0393/17/5/055003.

[52] See supplementary material, (n.d.).

[53] Y. Le Page, P. Saxe, Symmetry-general least-squares extraction of elastic coefficients from ab initio total energy calculations, Phys. Rev. B. 63 (2001) 174103.

[54] Y. Le Page, P. Saxe, Symmetry-general least-squares extraction of elastic data for strained materials from ab initio calculations of stress, Phys. Rev. B. 65 (2002) 104104.

[55] M. Moakher, A.N. Norris, The closest elastic tensor of arbitrary symmetry to an elasticity tensor of lower symmetr, J. Elast. 85 (2006) 215–263.

[56] J.T. Browaeys, S. Chevrot, Decomposition of the elastic tensor and geophysical applications, Geophys. J. Int. 159 (2004) 667–678.

[57] P. Djemia, C. Dugautier, T. Chauveau, E. Dogheche, M.I. De Barros, L.

Vandenbulcke, Mechanical properties of diamond films: A comparative study of polycrystalline and smooth fine-grained diamonds by Brillouin light scattering, J. Appl. Phys. 90 (2001) 3771–3779. doi:10.1063/1.1402667.

[58] P. Djemia, F. Ganot, P. Moch, V. Branger, P. Goudeau, Brillouin scattering investigation of elastic properties of Cu–Mo solid solution thin films, J. Appl. Phys. 90 (2001) 756–762. doi:10.1063/1.1378331.

[59] A. Fillon, C. Jaouen, A. Michel, G. Abadias, C. Tromas, L. Belliard, B. Perrin, P. Djemia, Lattice instability and elastic response of metastable Mo1-xSix thin films, Phys. Rev. B. 88 (2013) 174104. doi:10.1103/PhysRevB.88.174104.

[60] R. Loudon, Theory of Surface-Ripple Brillouin Scattering by Solids, Phys. Rev. Lett. 40 (1978) 581–583. doi:10.1103/PhysRevLett.40.581.

[61] C. Thomsen, J. Strait, Z. Vardeny, H.J. Maris, J. Tauc, J.J. Hauser, Coherent Phonon Generation and Detection by Picosecond Light Pulses, Phys. Rev. Lett. 53 (1984) 989–992.

[62] F. Xu, L. Belliard, D. Fournier, E. Charron, J.-Y. Duquesne, S. Martin, C. Secouard, B. Perrin, Complete elastic characterization of lithium phosphorous oxynitride films using picosecond ultrasonics, Thin Solid Films. 548 (2013) 366–370. doi:10.1016/j.tsf.2013.08.080.

[63] L. Belliard, T.W. Cornelius, B. Perrin, N. Kacemi, L. Becerra, O. Thomas, M. Eugenia Toimil-Molares, M. Cassinelli, Vibrational response of free standing single copper nanowire through transient reflectivity microscopy, J. Appl. Phys. 114 (2013) 193509. doi:10.1063/1.4831957.

[64] C.S. Shin, D. Gall, P. Desjardins, A. Vailionis, H. Kim, I. Petrov, J.E. Greene, M. Odén, Growth and physical properties of epitaxial metastable cubic TaN(001), Appl. Phys. Lett. 75 (1999) 3808–3810. doi:10.1063/1.125463.

[65] H. Wang, A. Tiwari, A. Kvit, X. Zhang, J. Narayan, Epitaxial growth of TaN thin films on Si(100) and Si(111) using a TiN buffer layer, Appl. Phys. Lett. 80 (2002) 2323–2325. doi:10.1063/1.1466522.

[66] C.S. Shin, D. Gall, Y.W. Kim, P. Desjardins, I. Petrov, J.E. Greene, M. Odén, L. Hultman, Epitaxial NaCl structure δ-TaNx(001): Electronic transport properties, elastic modulus, and hardness versus N/Ta ratio, J. Appl. Phys. 90 (2001) 2879–2885. doi:10.1063/1.1391214.

[67] J.L. Schroeder, A.S. Ingason, J. Rosén, J. Birch, Beware of poor-quality MgO substrates: A study of MgO substrate quality and its effect on thin film quality, J.

Cryst. Growth. 420 (2015) 22–31. doi:10.1016/j.jcrysgro.2015.03.010.

[68] M. Budde, C. Tschammer, P. Franz, J. Feldl, M. Ramsteiner, R. Goldhahn, M. Feneberg, N. Barsan, A. Oprea, O. Bierwagen, Structural, optical, and electrical properties of unintentionally doped NiO layers grown on MgO by plasma-assisted molecular beam epitaxy, J. Appl. Phys. 123 (2018) 195301. doi:10.1063/1.5026738.

[69] A.B. Mei, R.B. Wilson, D. Li, D.G. Cahill, A. Rockett, J. Birch, L. Hultman, J.E. Greene, I. Petrov, Elastic constants, Poisson ratios, and the elastic anisotropy of VN(001), (011), and (111) epitaxial layers grown by reactive magnetron sputter deposition, J. Appl. Phys. 115 (2014) 214908. doi:10.1063/1.4881817.

[70] S.J. Lloyd, D.M. Thicker, Z.H. Barber, M.G. Blamire, Growth of niobium nitride/aluminium nitride trilayers and multilayers, Philos. Mag. A Phys. Condens. Matter, Struct. Defects Mech. Prop. 81 (2001) 2317–2335. doi:10.1080/01418610108217151.

[71] L.E. Koutsokeras, G. Abadias, P. Patsalas, Texture and microstructure evolution in single-phase TixTa1−xN alloys of rocksalt structure, J. Appl. Phys. 110 (2011) 043535. doi:10.1063/1.3622585.

[72] G.M. Matenoglou, L.E. Koutsokeras, C.E. Lekka, G. Abadias, S. Camelio, G.A. Evangelakis, C. Kosmidis, P. Patsalas, Optical properties, structural parameters, and bonding of highly textured rocksalt tantalum nitride films, J. Appl. Phys. 104 (2008) 124907. doi:10.1063/1.3043882.

[73] H.B. Nie, S.Y. Xu, S.J. Wang, L.P. You, Z. Yang, C.K. Ong, J. Li, T.Y.F. Liew, Structural and electrical properties of tantalum nitride thin films fabricated by using reactive radio-frequency magnetron sputtering, Appl. Phys. A Mater. Sci. Process. 73 (2001) 229–236. doi:10.1007/s003390000691.

[74] B.I.P. Parkin, A. Rowley, Solid-State Routes to Tantalum Nitrides (TaN, Ta3N5), Adv. Mater. 6 (1994) 780–782. doi:10.1007/978-3-319-78919-4.

[75] G. Abadias, L.E.E. Koutsokeras, P. Guerin, P. Patsalas, Stress evolution in magnetron sputtered Ti-Zr-N and Ti-Ta-N films studied by in situ wafer curvature: Role of energetic particles, Thin Solid Films. 518 (2009) 1532–1537. doi:10.1016/j.tsf.2009.07.183.

[76] P. Patsalas, C. Gravalidis, S. Logothetidis, Surface kinetics and subplantation phenomena affecting the texture, morphology, stress, and growth evolution of titanium nitride films, J. Appl. Phys. 96 (2004) 6234–6235. doi:10.1063/1.1811389.

[77] G. Abadias, L.E. Koutsokeras, A. Siozios, P. Patsalas, Stress, phase stability and

oxidation resistance of ternary Ti-Me-N (Me = Zr, Ta) hard coatings, Thin Solid Films. 538 (2013) 56–70.

[78] L.E. Koutsokeras, G. Abadias, C.E. Lekka, G.M. Matenoglou, D.F. Anagnostopoulos, G.A. Evangelakis, P. Patsalas, Conducting transition metal nitride thin films with tailored cell sizes: The case of δ- Tix Ta1-x N, Appl. Phys. Lett. 93 (2008) 011904. doi:10.1063/1.2955838.

[79] K. Zhang, K. Balasubramanian, B.D. Ozsdolay, C.P. Mulligan, S. V. Khare, W.T. Zheng, D. Gall, Growth and mechanical properties of epitaxial NbN(001) films on MgO(001), Surf. Coatings Technol. 288 (2016) 105–114. doi:10.1016/j.surfcoat.2016.01.009.

[80] S. Hu, C. Xu, Y. Lao, Y. Wang, H. Zhang, G.J. Zhang, J. Yang, The stabilization of the rocksalt structured tantalum nitride, J. Appl. Phys. 122 (2017) 045109. doi:10.1063/1.4989415.

[81] F.F. Klimashin, N. Koutnà, H. Euchner, D. Holec, P.H. Mayrhofer, N. Koutná, H. Euchner, D. Holec, P.H. Mayrhofer, The impact of nitrogen content and vacancies on structure and mechanical properties of Mo-N thin films, J. Appl. Phys. 120 (2016) 185301. doi:10.1063/1.4966664.

[82] C. Stampfl, A.J. Freeman, Metallic to insulating nature of TaNx: Role of Ta and N vacancies, Phys. Rev. B. 67 (2003) 064108. doi:10.1103/PhysRevB.67.064108.

[83] M. Grumski, P.P. Dholabhai, J.B. Adams, Ab initio study of the stable phases of 1:1 tantalum nitride, Acta Mater. 61 (2013) 3799–3807. doi:10.1016/j.actamat.2013.03.018.

[84] Z. Gu, C. Hu, X. Fan, L. Xu, M. Wen, Q. Meng, L. Zhao, X. Zheng, W. Zheng, On the nature of point defect and its effect on electronic structure of rocksalt hafnium nitride films, Acta Mater. 81 (2014) 315–325. doi:10.1016/j.actamat.2014.08.040.

[85] the mass density derived from XRD, ρ_{XRD}, was calculated using the equation $\rho_{XRD} = \frac{M}{a_0^3}$, where M is the mass of the unit cell given by $M = 4[M_{Ta}(1 - c_{Ta}) + M_N(1 - c_N)]/\mathcal{N}_a$ with c_{Ta} and c_N the vacancy concentration on Ta and N sites, M_{Ta}= 180.95 g/mol, M_N=14.00 g/mol, $\mathcal{N}_a$ is the Avogadro number, and a_0 the stress-free lattice parameter.

[86] B.D. Ozsdolay, C.P. Mulligan, M. Guerette, L. Huang, D. Gall, Epitaxial growth and properties of cubic WN on MgO(001), MgO(111), and Al2O3(0001), Thin Solid Films. 590 (2015) 276–283. doi:10.1016/j.tsf.2015.08.002.

[87] B.D. Ozsdolay, C.P. Mulligan, K. Balasubramanian, L. Huang, S. V. Khare, D. Gall,

Cubic β-WNxlayers: Growth and properties vs N-to-W ratio, Surf. Coatings Technol. 304 (2016) 98–107. doi:10.1016/j.surfcoat.2016.06.079.

[88] S.-H. Jhi, S.G. Louie, M.L. Cohen, J. Ihm, Vacancy Hardening and Softening in Transition Metal Carbides and Nitrides, Phys. Rev. Lett. 86 (2001) 3348–3351. doi:10.1103/PhysRevLett.86.3348.

[89] Note that main XRD lines of P4/nmm TaN phase coincide with those of cubic Fm-3m TaN phase, see Ref. 80, (n.d.).

[90] F. Mouhat, F.-X. Coudert, Necessary and sufficient elastic stability conditions in various crystal systems, Phys. Rev. B. 90 (2014) 224104. doi:10.1103/PhysRevB.90.224104.

[91] A. Togo, I. Tanaka, First principles phonon calculations in materials science, Scr. Mater. 108 (2015) 1–5. doi:10.1016/J.SCRIPTAMAT.2015.07.021.

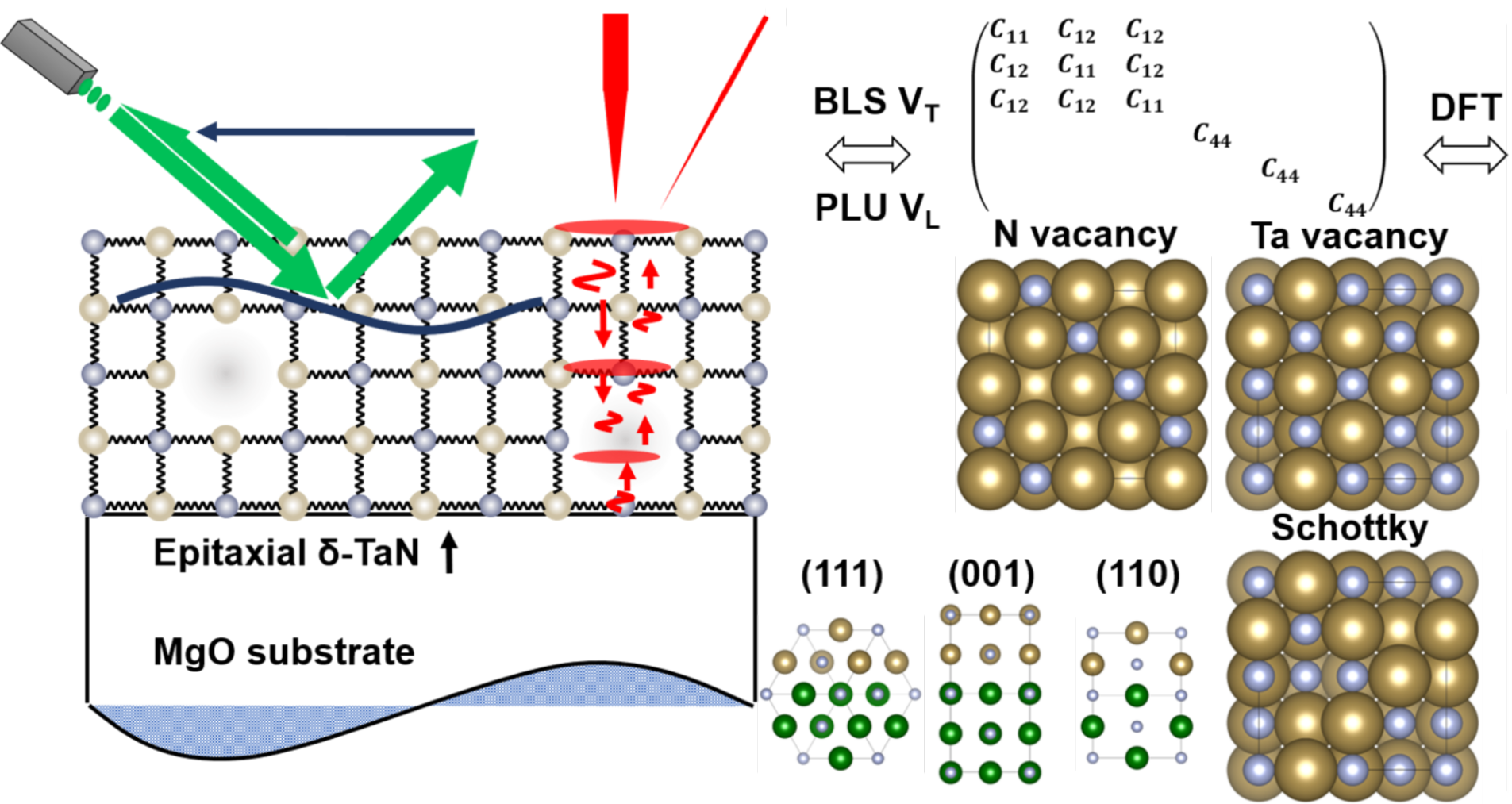

BLS V_T ⟺ PLU V_L

$$\begin{pmatrix} C_{11} & C_{12} & C_{12} & & & \\ C_{12} & C_{11} & C_{12} & & & \\ C_{12} & C_{12} & C_{11} & & & \\ & & & C_{44} & & \\ & & & & C_{44} & \\ & & & & & C_{44} \end{pmatrix}$$

⟺ DFT